https://doi.org/10.5194/essd-2026-40
Preprint. Discussion started: 15 April 2026

Open Access Earth System Science Data Discussions

EGO: a global 0.05° hourly GPP dataset for monitoring diurnal photosynthesis dynamics

Xi Liu[1], Xing Li[1], Dalei Hao[2], Jingfeng Xiao[3], Yanan Zhou[1], Cenliang Zhao[1], Zikang Diao[1], Fuqiang Qu[1], Shangrong Lin[1], Xiangzhuo Liu[4], Zhaoying Zhang[5], Xinjie Liu[6], Helin Zhang[7]

1 School of Geography and Planning, Sun Yat-sen University, Guangzhou 510006, China
2 Atmospheric, Climate, & Earth Sciences Division, Pacific Northwest National Laboratory, 902 Battelle Blvd, Richland, WA 99354, USA
3 Earth Systems Research Center, Institute for the Study of Earth, Oceans, and Space, University of New Hampshire, Durham, NH 03824, USA
4 INRAE, Bordeaux Sciences Agro, UMR 1391 ISPA, Villenave-d'Ornon, France
5 International Institute for Earth System Sciences, Jiangsu Center for Collaborative Innovation in Geographical Information Resource Development and Application, Nanjing University, Nanjing, Jiangsu 210023, China
6 Key Laboratory of Digital Earth Science, Aerospace Information Research Institute, Chinese Academy of Sciences, 100094 Beijing, China
7 Research Institute of Agriculture and Life Sciences, Seoul National University, Seoul 08826, Republic of Korea

Correspondence to: Xing Li (lixing58@mail.sysu.edu.cn);

Abstract. Vegetation photosynthesis, quantified as gross primary productivity (GPP), regulates the terrestrial carbon sink and land–atmosphere exchanges. At sub-daily scales, diurnal GPP dynamics reveal rapid adjustments to changing light, temperature and water conditions that are largely obscured in daily-to-annual aggregates, underscoring the need for developing global hourly GPP products. However, existing hourly products mostly rely on traditional machine-learning schemes that lack explicit biophysical constraints and an adequate representation of water limitation, leading to large uncertainties, especially in arid regions. Besides, the added value of hourly products for resolving diurnal behavior and responses to environmental stress remains poorly quantified. Here, we develop a causal knowledge-driven upscaling framework that couples the Peter and Clark Momentary Conditional Independence guided causal weights with ensemble learning strategies. Based on eddy-covariance measurements and multi-source meteorological variables, vegetation properties, and land-cover fields, we generated a global 0.05° hourly GPP product from 2000 to 2022, named EGO (Eddy covariance site-based Global hOurly) GPP, and then evaluated how well EGO reproduces observed diurnal cycles and their responses to extreme events. EGO GPP achieves an R^2 of 0.76 and an RMSE of 4.17 μmol CO_2 m^{-2} s^{-1} on independent test sites, and outperforms two recent hourly upscaling products (FLUXCOM and X-BASE; $R^2 \approx 0.60$ and RMSE ≈ 5.5 μmol CO_2 m^{-2} s^{-1}), with large improvement in drylands. EGO GPP clearly illustrates the diurnal progression of photosynthesis and captures observed diurnal metrics across diverse biomes, revealing strong midday depression and morning-skewed curves in drylands but near-symmetric cycles in high-latitude and humid tropical regions. Analyses of the June 2021 U.S. drought and the August 2003 European heatwave further show that EGO reliably tracks diurnal photosynthetic responses to extremes, including GPP reductions, earlier centroid/peak times and intensified midday depression, consistent with tower-based results. Looking ahead, EGO GPP provides a reliable foundation

for investigating diurnal photosynthetic behavior, exploring vegetation–climate interactions and benchmarking Earth system models at a sub-daily scale. EGO GPP is available at https://doi.org/10.5281/zenodo.18253238 (Liu et al., 2026).

1 Introduction

Vegetation assimilates atmospheric CO_2 into organic carbon through photosynthesis, forming the largest carbon flux between the biosphere and the atmosphere (Ruehr et al., 2023). Gross primary productivity (GPP), a key indicator of photosynthetic activity, is widely used to quantify the carbon sequestration capacity of terrestrial ecosystems (Beer et al., 2010). Existing studies have investigated GPP dynamics across multiple temporal scales, from annual and monthly to daily and sub-daily (Ryu et al., 2019; Xiao et al., 2021). Analyses at longer timescales (e.g., daily, monthly and annual) provide valuable insights into photosynthetic phenology and interannual variability (Wang et al., 2025). In contrast, shorter scales (e.g., sub-daily or hourly) focus on how vegetation photosynthesis responds to instantaneous changes in light, temperature, and water availability within a day (Ruehr et al., 2024). These short-term dynamics reveal rapid physiological regulation of vegetation, particularly via stomatal conductance, offering a unique window into the mechanisms of vegetation–environment interactions. Early flux tower-based studies showed that short-term variations in environmental factors can induce pronounced diurnal fluctuations in vegetation photosynthesis, that are often obscured in longer-timescale analyses (Nelson et al., 2018). More recently, advances in remote sensing, especially the emergence of new-generation geostationary satellites, have enabled regional-scale studies that report several key physiological phenomena occurring at sub-daily timescales, including midday depression or increasing diurnal asymmetry in photosynthesis under stress (Li et al., 2023; Xiao et al., 2021; Zhang et al., 2023). These studies extend beyond the spatial coverage of traditional tower-based monitoring, allowing diurnal dynamics to be characterized across broader regions. Nevertheless, current investigations remain largely confined to site or regional scales, limiting our understanding of diurnal photosynthetic behavior across global ecosystems. Consequently, monitoring the diurnal dynamics of vegetation photosynthesis at the global scale has become a key prerequisite for uncovering the general mechanisms that govern photosynthetic behavior and its responses to environment.

Polar-orbiting satellites provide near-global coverage and have therefore become the primary tools for generating global GPP products, such as the Moderate Resolution Imaging Spectroradiometer (MODIS) and Advanced Very High Resolution Radiometer (AVHRR) (Robinson et al., 2018; Xiao et al., 2019; Zhao et al., 2005). However, their sun-synchronous orbits provide only instantaneous snapshots at fixed overpass times, making it difficult to resolve continuous diurnal course of photosynthesis and fundamentally limiting their applicability for sub-daily studies. In recent years, new-generation geostationary satellites, including the Geostationary Operational Environmental Satellite, Himawari-8/9, and GK-2A etc., provide high-frequency, continuous observations, and have been used to monitor diurnal variations in photosynthesis, but their coverage is restricted to specific regions, preventing truly global monitoring (Jeong et al., 2023; Li et al., 2023; Zhang et al., 2023). In parallel, the OCO-3 instrument onboard the International Space Station measures solar-induced chlorophyll fluorescence (SIF), a proxy for GPP, at varying local times, offering new opportunities to sample diurnal photosynthetic dynamics from space (Stavros et al., 2017; Taylor et al., 2020). Nevertheless, OCO-3 footprints are sparse and discontinuous in both space and time, which poses challenges for constructing continuous global maps of diurnal photosynthesis (Deng et al., 2025; Liu et al., 2025; Zhang et al., 2023). Unlike these satellite observations, eddy-covariance (EC) flux towers measure the turbulent exchange of carbon, water, and energy between ecosystems and atmosphere directly, providing near-continuous records at half-hourly or hourly resolution over multi-decadal periods (Xiao et al., 2025). They are widely regarded as the gold standard for flux measurements and remain the primary benchmark for validating gridded GPP products (Wang et al., 2025). Although global flux networks such as FLUXNET comprise hundreds of sites, their spatial distribution and ecosystem representativeness remain highly uneven, making regional or global scale assessments challenging (Pastorello et al., 2020).

To overcome this challenge, machine-learning upscaling approaches based on EC measurements have demonstrated strong capabilities (Ichii et al., 2017). They learn complex relationships between environmental variables and GPP from large observations datasets and can then be extrapolated globally. A prominent example is FLUXCOM, the first global GPP product derived from machine-learning upscaling method (Bodesheim et al., 2018). In its early version, FLUXCOM relied mainly on sub-daily radiation to drive the diurnal GPP cycle, since other hourly input variables were not yet available, inevitably overlooking short-term variability in environmental drivers such as temperature and water conditions. More recently, the FLUXCOM team incorporated hourly meteorological data from ERA5 and released X-BASE, which improved the robustness of upscaling framework (Nelson et al., 2024). However, even with these updates, certain limitations remain. As reported in Nelson et al., (2024), this product exhibits considerable uncertainty in arid regions and a limited ability to capture water-related effects on diurnal photosynthesis. A plausible explanation is that the current predictor set does not fully represent the multiple dimensions of water limitation, even though both short-term water availability and long-term water balance strongly regulate ecosystem productivity and drought sensitivity in drylands (Liu et al., 2025). Beyond the choice of input variables, the modeling framework itself presents an additional challenge. Diurnal vegetation photosynthesis emerges from complex interactions among biophysical and biochemical processes. Conventional machine learning models can capture non-linear relationships among many inputs, but their purely correlational nature limits direct process interpretation and raises questions about robustness under novel environmental conditions (Runge et al., 2019).

Recently, approaches that combine causal inference with machine learning offer a promising pathway to better learn the complex relationships between environmental drivers and ecosystem fluxes (Kretschmer et al., 2021). Traditional machine learning models typically rely on correlations rather than directional causal relationships (Yuan et al., 2022). Without causal guidance, these models risk capturing spurious associations driven by confounding factors such as predictors sharing similar variations, which can render predictions unreliable (Galytska et al., 2023). As one of the state-of-the-art causal inference methods, the PCMCI (Peter and Clark Momentary Conditional Independence) offers a robust solution especially suitable for

https://doi.org/10.5194/essd-2026-40
Preprint. Discussion started: 15 April 2026

earth science applications, as it rigorously filters out confounding effects to identify true causal pathways (Li et al., 2021; Runge et al., 2023). Another benefit is its ability to represent time-lagged dependencies, which is critical for estimating hourly GPP, since previous research has highlighted that vegetation photosynthesis exhibits certain lagged responses to environmental fluctuations in sub-daily (Krich et al., 2020). By embedding the causal structure into machine learning models, PCMCI acts as a form of biophysical constraint that guides model training (Runge et al., 2023; Yuan et al., 2024). This strategy helps clarify the causal pathways between predictors and GPP and has the potential to improve the model's predictive accuracy and robustness. Recent applications of PCMCI in flux upscaling have shown encouraging results, for instance, Zhao and Zhu (2025) combined PCMCI with XGBoost to generate a global monthly ecosystem respiration product, which improved estimation accuracy by aligning model weight with causal pathways.

One additional important issue concerns the evaluation of hourly GPP products. Previous product-oriented studies rely on aggregated metrics such as coefficient of determination (R^2), root mean square error (RMSE), and bias (Bias), focusing on overall agreement with observations while providing little information on how well products reproduce diurnal shape of photosynthesis (Bodesheim et al., 2018; Leng et al., 2024; Li et al., 2025; Zhang et al., 2023). Yet the added value of hourly GPP lies precisely in its ability to resolve intra-day variations. Recent studies have revealed distinct diurnal features of vegetation photosynthesis, including global-scale morning–afternoon asymmetry (Liu et al., 2024), pronounced midday depression in mangrove ecosystems (Zhu and Zhu, 2025), and heatwave-induced advances of daily photosynthetic peak by 2–3 hours in dryland regions (Li et al., 2023). Demonstrating the capacities of the new hourly GPP products in capturing these environment-driven diurnal shifts is essential for their widespread use in global change studies.

Here, we develop a new global hourly GPP product using a causal-constrained machine-learning framework based on EC-site measurements. We combine a multi-dimensional set of predictors, including meteorological variables, vegetation properties and indicators of both short-term and long-term water availability, in order to more fully represent vegetation–environment interactions, and then conduct a multi-faceted evaluation of the product's ability to reproduce key diurnal features of photosynthesis. Specifically, we aim to 1) produce a global 0.05°, hourly GPP product upscaled from flux-tower observations and assess its overall accuracy and robustness, 2) evaluate how well the product characterizes diurnal photosynthetic dynamics, and 3) examine the capability of the product in capturing vegetation diurnal response to extreme climatic events. The resulting product is intended to provide a valuable resource for diurnal global carbon-cycle studies, to enable more accurate characterization of short-term vegetation–climate interactions, and to offer an observational benchmark for evaluating Earth system model simulations at sub-daily time scale.

2 Data

This study combined multi-source from ground-based, satellite and reanalysis datasets to develop a global hourly GPP product.

https://doi.org/10.5194/essd-2026-40
Preprint. Discussion started: 15 April 2026

EC measurements from 190 flux sites served as the primary reference for model training and validation, providing site-level benchmarks for ecosystem photosynthesis. As predictors, we used a suite of global gridded datasets of environmental, vegetation and land-cover variables for mapping hour GPP globally, and further compared our product with two existing hourly upscaled GPP datasets (FLUXCOM and X-BASE) in terms of overall accuracy, diurnal dynamics and spatial patterns.

2.1 Eddy covariance data

The FLUXNET2015 Tier 1 dataset (https://fluxnet.org/), spanning approximately 1990–2014, integrates long-term EC flux observations from multiple regional networks worldwide and provides harmonized tower data after standardized flux partitioning, quality control, and gap-filling (Pastorello et al., 2020). To further expand the training samples for modelling, we additionally incorporated data from AmeriFlux (https://ameriflux.lbl.gov/), covering ~1990 to the present (data up to 2022 were used), that follow the same processing pipelines with FLUXNET (Chu et al., 2023). Given that the footprint of EC observations differs from the 0.05° grid of the upscaled product, we applied additional filtering to reduce scale mismatch. We first used the MODIS land cover product (MCD12Q1 Version 6.1 with 500 m resolution, covering 2001–2022) and reclassified its vegetation types following the scheme in Table S1 to ensure consistency with the flux-site classification. The reclassified data were then resampled to 0.05° spatial resolution, and the dominant vegetation type within each grid cell was retained. We kept only those flux sites whose vegetation type consistently matched the dominant class of their corresponding 0.05° grid cell throughout all available years, resulting in a total of 190 representative sites selected from 316 available sites across diverse vegetation types and Whittaker biomes (Fig. 1, Table S1).

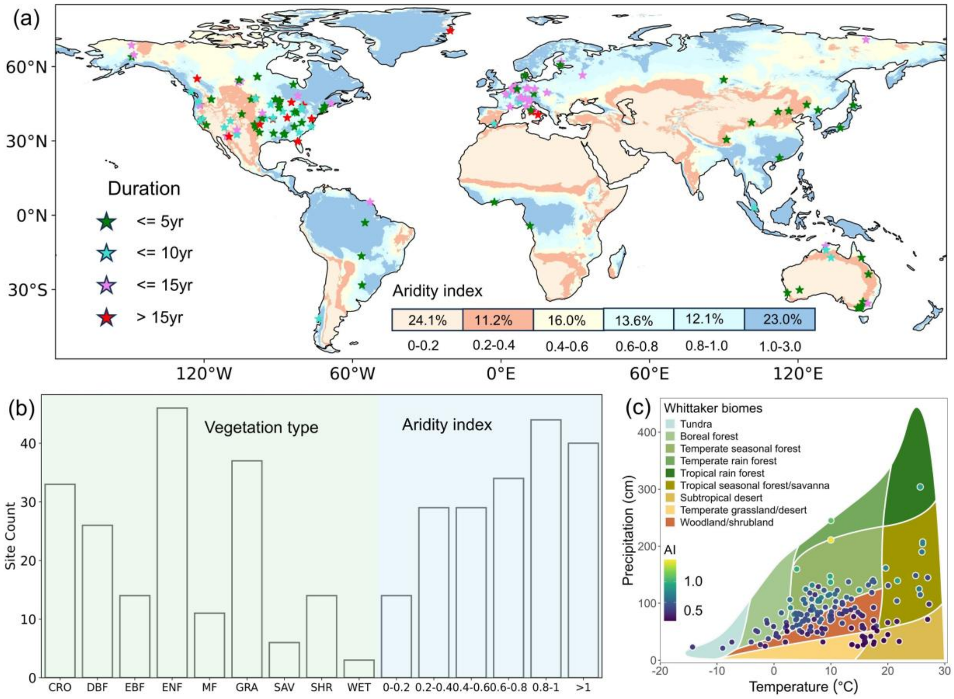

Figure 1. (a) Spatial distribution of the 190 eddy covariance flux sites used in this study. The background map shows the global aridity index, and the color bar indicates the proportion of land area within each aridity class. Sites with different observation durations are marked by star symbols in different colors. (b) Number of sites categorized by vegetation type and aridity gradient. (c) Distribution of sites across the Whittaker biome classification, where each site is positioned according to its mean annual temperature and precipitation. Vegetation type abbreviations are as follows: cropland (CRO), deciduous broadleaf forest (DBF), evergreen broadleaf forest (EBF), evergreen needleleaf forest (ENF), mixed forest (MF), grassland (GRA), savannas (SAV), shrubland (SHR) and wetland (WET).

To ensure data quality for model training and evaluation, we applied the following procedures to the tower-based GPP (GPP_NT_VUT): (1) removed negative values that are physiologically unrealistic; (2) retained only records with quality-control flags equal to 0 or 1; and (3) converted all timestamps to local solar time (LST) to remove phase shifts related to solar position and ensure physical consistency of diurnal variations (see Text S1 for details).

2.2 Global gridded datasets

2.2.1 Environmental variables

For climate forcing, we used the ERA5-Land reanalysis dataset (0.1°) from the European Centre for Medium-Range Weather Forecasts (ECMWF), which provides global hourly fields of incoming shortwave radiation (SW), air temperature (Ta), 0–100 cm soil water content (SWC), and dew point temperature (Table S2) (Munoz-Sabater et al., 2021). Based on 2 meters air temperature and 2 meters dew point temperature, we calculated hourly vapor pressure deficit (VPD) to quantify atmospheric dryness relevant for photosynthetic regulation (see Text S2 for details). The aridity index was obtained from the Global-AI_PET_v3 dataset and defined as mean annual precipitation divided by potential evapotranspiration over the climatological baseline, thereby characterizing long-term water availability across ecosystems (Zomer et al., 2022). Regions with $AI<0.65$ were classified as drylands, and all others as non-drylands (Koppa et al., 2024). To account for the influence of atmospheric CO2 concentration on photosynthesis, we used global 3-hourly CO2 concentration data at 3° × 2° from the NOAA CarbonTracker (http://carbontracker.noaa.gov) and applied time-weighted interpolation to generate continuous hourly CO2 series (Chen et al., 2019). Given the distinct effects of diffuse (PARDF) and direct (PARDR) radiation on light use efficiency and GPP (Wang et al., 2023), we included the diffuse radiation fraction (DRF) as an additional predictor, computed from MERRA-2 hourly PARDF and PARDR (M2T1NXLFO; 0.5° × 0.625°) as $DRF = PARDF / (PARDF + PARDR)$.

2.2.2 Satellite datasets

We integrated multiple satellite datasets from MODIS platform. The MODIS MCD43C4 dataset provides daily Bidirectional Reflectance Distribution Function (BRDF)-adjusted global nadir surface reflectance at 0.05° resolution, which reduces the influence of viewing geometry and solar zenith angle. Using the red, near-infrared, blue, and shortwave infrared bands, we calculated enhanced vegetation index (EVI) and land surface water index (LSWI) to represent canopy greenness and surface moisture condition, respectively (see Text S3 for details) (Huete et al., 2002; Zeng et al., 2022). Additionally, we obtained the clumping index (CI) from the CAS-CI product and leaf area index (LAI) from the MODIS MOD15A2H Version 6.1 to further characterize the canopy structure (Wei et al., 2019). Here, we assumed that these vegetation structural parameters remain relatively stable throughout the diurnal cycle (Bodesheim et al., 2018; Leng et al., 2024).

Vegetation type information was derived from the MCD12Q1 Version 6.1 based on the International Geosphere-Biosphere Program (IGBP) classification at 500 m resolution. To align with our ecosystem modelling framework, the original IGBP classes were reclassified into a simplified scheme: forests (evergreen needleleaf forest, evergreen broadleaf forest, deciduous needleleaf forest, deciduous broadleaf forest, and mixed forest), shrublands (closed and open shrubland), savannas (woody savannas and savannas), and separate classes for grassland, cropland, and wetland. Detailed reclassification rules are listed in Table S1. To represent sub-grid landscape heterogeneity and reduce uncertainty from mixed pixels, we calculated the fractional coverage of each vegetation type within every 0.05° grid cell, denoting these variables as fraction of forest (FFO), shrubland (FSH), savannas (FSA), grassland (FGR), cropland (FCR), and wetland (FWE). Compared with using only the dominant class, this fractional representation provides a more nuanced description of vegetation composition and supports more detailed and accurate spatial upscaling across biomes. The benefit of this strategy can be found in Text S4 and Fig.S1 for more detail.

2.3 Hourly upscaled GPP products for comparison

To comprehensively evaluate the performance of our hourly GPP product, we compared it with two recently developed hourly GPP products that are also generated via machine-learning-based upscaling strategies. The first is FLUXCOM (Bodesheim et al., 2018), a pioneering upscaling product that provides global GPP at 0.5° resolution for 2001–2014; The second is X-BASE, a global 0.25° GPP product developed under the recent FLUXCOM-X framework covering 2001–2021 (Nelson et al., 2024). To our knowledge, these two products are the only currently available global hourly GPP that upscaled from in-situ eddy covariance measurements and represent the efforts in this field. All products were evaluated against site-level GPP, focusing on overall accuracy, representation of diurnal cycles, and spatiotemporal patterns.

3 Methodology

3.1 Feature selection

Prior to modeling, we performed feature selection to reduce the influence of redundant predictors (Fig. 2). Owing to its robust screening strategy, Boruta is particularly suitable for high-dimensional and multi-source modelling tasks (Kursa and Rudnicki, 2010). The algorithm operates by creating shadow features to establish a baseline. Through iterative testing, predictors with lower importance than their corresponding shadow features are removed. We implemented this process using the BorutaPy package in Scikit-learn with 100 iterations to ensure result stability. As shown in Fig. S2, the clumping index and LAI were discarded, indicating that their information was likely redundantly captured by EVI. The remaining predictors were then evaluated for multicollinearity using the variance inflation factor (VIF). The results showed that all retained predictors satisfied the collinearity criterion (VIF < 10) and were therefore used in subsequent modelling (Table S3). The final set of global gridded predictors used for modelling and upscaling is listed in TableS2.

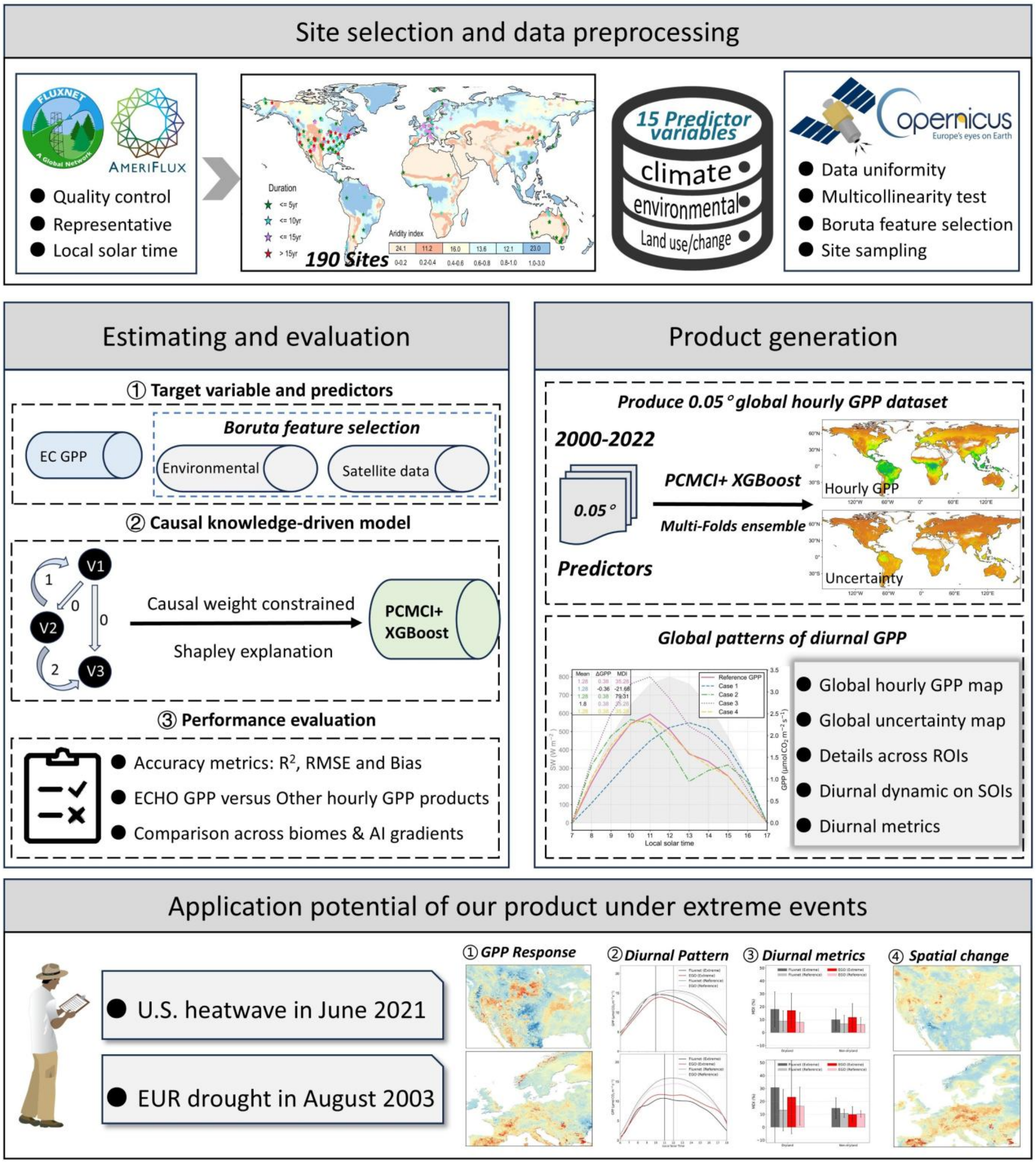

Figure 2. Workflow for generating the EGO (Eddy covariance site-based Global hOurly) GPP, encompassing data processing, model training, evaluation, and application assessment.

3.2 Predicting and upscaling

3.2.1 CKML-GPP model

We used a Causal Knowledge-driven Machine Learning model (CKML-GPP) to simulate hourly GPP, which integrates the powerful nonlinear regression capabilities of EXtreme Gradient Boosting (XGBoost) with the rigorous causal inference framework of PCMCI (Yuan et al., 2024; Zhao and Zhu, 2025). The PCMCI algorithm is particularly well-suited for earth science applications as it effectively infers multivariate controls and time-lagged causal relationships in high-dimensional time series (Runge et al., 2023). It operates in two distinct stages: the PC algorithm (named after Peter Spirtes and Clark Glymour) and the Momentary Conditional Independence (MCI) test. First, the PC step iteratively filters the initial predictor pool to identify a reduced set of relevant necessary confounders for each variable. Then, the MCI test quantifies the causal strength and detects time-lagged dependencies between predictors and the target variable by conditioning on these identified parents to remove confounding effects. This two-step approach substantially enhances causal detection power by avoiding the statistical challenges of conditioning on high-dimensional variables.

In CKML-GPP, the causal structure identified by PCMCI serves as a physical constraint to guide the XGBoost training process. Specifically, causal weights derived from the MCI step are used to dynamically adjust the probability that each predictor is selected as a decision node in the tree structure. Predictors with stronger causal effects are assigned higher selection probabilities, so that the resulting model structure more closely reflects the dominant drivers of vegetation photosynthetic diurnal dynamics. To further enhance model performance and avoid subjective bias, we employed the Particle Swarm Optimization (PSO) algorithm to automatically search for the global optimum of hyperparameters (Ishaque and Salam, 2013). In addition, to address potential uncertainties arising from grid-based input data during model training, we conducted additional experiments in which CKML-GPP was retrained using variables directly observed at the flux towers. This comparison enabled an assessment of model's sensitivity to input data quality. Finally, we used the SHAP (SHapley Additive exPlanations) method to interpret the feature contributions of CKML-GPP, quantifying both the magnitude and direction of each environmental variable’s influence on hourly GPP variation (Zhang et al., 2024).

3.2.2 Model training and evaluation

Before model training, all driving variables were harmonized in both spatial and temporal resolutions. Temporally, all input variables were converted to local solar time to ensure that the estimated GPP corresponded to the natural local diurnal cycle of vegetation. Spatially, all variables were resampled to a uniform 0.05° resolution. We adopted a 10-fold site-wise cross-validation strategy to train and evaluate the CKML-GPP model. Specifically, the available sites were randomly partitioned into 10 distinct subsets. In each iteration, nine subsets served as the training set, while the remaining one was used for testing. This procedure was rotated 10 times to ensure that every site functioned as an independent test sample exactly once, allowing us to compile a comprehensive validation dataset covering all sites. Furthermore, to mitigate the impact of random initialization and ensure result stability, we performed 20 independent runs with different random seeds for each fold. The final prediction for each test sample was derived from the ensemble average of these 20 runs. Model performance was systematically evaluated against tower GPP across vegetation types and aridity gradients. The evaluation metrics included the R^2, RMSE, and bias. The detailed formulas for each metrics are given in Text S5.

3.2.3 Global mapping of hourly GPP

For each grid cell, the final GPP estimate was obtained by averaging the outputs from the 10-fold cross-validation models. For each fold, 20 independent runs with different random seeds were conducted, and the median prediction was taken as the fold output. This ensemble strategy, following previous studies, effectively reduces prediction uncertainty (Nathaniel et al., 2023). The resulting dataset is named EGO (Eddy covariance site-based Global hOurly) GPP. Considering computational efficiency and practical applicability, we generated global monthly-averaged hourly GPP from 2000 to 2022 at 0.05° resolution for local solar times from 06:00 to 18:00. Benefiting from the multi-fold training framework, model uncertainty (expressed as the standard deviation among 10-fold predictions) was also calculated (Fig. 2). In addition, we present globally aggregated multi-year diurnal GPP maps from EGO and two other products and further selected three regions of interest (ROI) for detailed analysis (including the Amazon, the United States and Europe), enabling a comparative evaluation of spatial representational capability at both global and regional scales.

3.3 Diurnal metrics

To quantify the diurnal dynamics of vegetation photosynthesis, we used a set of metrics that describe the GPP diurnal curve from three complementary perspectives: absolute magnitude, diurnal asymmetry, and midday depression.

First, the absolute magnitude was defined as the mean GPP during the period from 6:00 to 18:00, reflecting the average intensity of daytime photosynthetic activity.

Second, diurnal asymmetry describes the difference in photosynthetic activity between morning and afternoon (Liu et al., 2024). This behavior is commonly quantified using metrics such as ΔGPP, diurnal centroid, and peak time. In this study, ΔGPP was used as the primary asymmetry metric and was calculated as:

$$\Delta\mathrm{GPP} = \frac{\mathrm{GPP_{AM}} - \mathrm{GPP_{PM}}}{\mathrm{GPP_{AM}}} \times 100\% \qquad (1)$$

where GPP_{AM} and GPP_{PM} denote the mean GPP during the morning (6:00–12:00) and afternoon (12:00–18:00), respectively. The diurnal centroid and peak time were used as supplementary indicators (Li et al., 2023; Wilson et al., 2003), a centroid or peak time occurring before noon indicates higher GPP in the morning than in the afternoon.

Finally, we introduced the midday depression intensity (MDI) to quantify the reduction in photosynthesis around midday (10:00–14:00), which reflects the physiological response of vegetation to stress. Based on the approach developed by (Zhu and Zhu, 2025), we calculated MDI as the normalized difference between the observed GPP curve and a hypothetical ideal GPP curve. Specifically, this ideal curve was constructed by modelling the theoretical linear relationship between GPP and solar radiation, thereby isolating physiological regulation from radiation-driven variations. MDI is calculated as:

$$\mathrm{MDI} = \frac{\sum_{t=10}^{t=14}\left(\mathrm{GPP_i(t)} - \mathrm{GPP_a(t)}\right)}{\sum_{t=10}^{t=14}\mathrm{GPP_a(t)}} \times 100\% \qquad (2)$$

where $GPP_i(t)$ and $GPP_a(t)$ are the actual and ideal GPP values at time t, respectively. A larger MDI indicates a greater deviation of actual GPP from the ideal curve and thus a stronger midday depression. To validate the sufficiency of these three metrics in capturing diurnal pattern, we conducted additional experiments, the details of which are presented in Text S6. Because these diurnal metrics are standardized, they are directly comparable across ecosystems and provide a consistent basis for global-scale analysis. Accordingly, we produced global maps of these diurnal indicators to visualize their spatial patterns. To assess how well different hourly GPP products capture diurnal dynamics, we constructed a three-dimensional metric space with mean GPP, ΔGPP, and MDI as the three axes. The distance between each product's data points and the site-based reference points in this metric space was used to quantify its ability to reproduce the observed diurnal variation patterns.

3.4 Performance of EGO GPP under extreme events

To assess how well EGO GPP captures diurnal vegetation photosynthesis under extreme climate conditions across ecosystems, we analyzed two well-documented extremes: the severe drought that occurred in the United States in June 2021 (Jiang et al., 2025) and the European heatwave in August 2003 (Garcia-Leon et al., 2021). For each case, we used flux tower observations with valid records for the corresponding months, covering the major ecosystem types in the U.S. and Europe, respectively. The evaluation consisted of two parts. To ensure a rigorous and independent assessment, we utilized the aggregated estimated GPP derived from the 10-fold cross-validation (i.e., the compilation of the 10 test sets), rather than the final upscaled product generated from the full dataset. Firstly, we quantified the accuracy of the estimated GPP during the extreme event. The estimated hourly GPP were paired with corresponding tower-based GPP, and GPP anomalies during the event periods were calculated for both datasets. Specifically, the anomaly was calculated as $(GPP_{extreme} - GPP_{reference}) / GPP_{reference}$, where $GPP_{extreme}$ represents the value during the specific event month, and $GPP_{reference}$ denotes the multi-year average for the same month excluding the event year. We then compared the R^2, RMSE, and bias to evaluate the consistency between EGO GPP and the observation. Second, we examined the ability of EGO GPP to reproduce diurnal photosynthetic dynamics under extreme events. For each period, we extracted diurnal curves from both the flux tower data and EGO GPP at each site. Using the metrics defined in Section 3.4, we derived diurnal metrics for every site and grouped them into dryland and non-dryland classes. The capacity of EGO GPP to represent stress-induced changes was evaluated by calculating the absolute difference in metrics between the event and reference periods (e.g., $MDI_{difference} = MDI_{extreme} - MDI_{reference}$). These differences were then compared with tower-based results to verify whether the EGO accurately captured the shifts in diurnal patterns.

4 Results

4.1 Estimating and evaluation of hourly GPP

Based on the established CKML-GPP model, we generated the global hourly upscaling product, EGO GPP, and then compared with FLUXCOM and X-BASE against EC flux GPP (Fig. 3). To ensure a fair comparison, all products were compared under identical conditions using only the test set samples for EGO (Section 3.2.2). Under this setup, EGO achieved an R^2 of 0.76 and an RMSE of 4.17 μmol CO_2 m^{-2} s^{-1}, outperforming the other products which show R^2 values around 0.60 and RMSE value around 5.5 μmol CO_2 m^{-2} s^{-1}. Regarding bias, both FLUXCOM and X-BASE exhibited systematically underestimation of GPP, with substantial negative biases of -2.35 and -2.33 μmol CO_2 m^{-2} s^{-1}, respectively. In contrast, EGO effectively mitigated this underestimation issue, reducing the bias to merely -0.36 μmol CO_2 m^{-2} s^{-1}. This improvement is also reflected in the regression slope (Fig. 3a-c), where FLUXCOM and X-BASE remain around 0.60, whereas EGO reaches 0.78. As shown in Fig. 3d, EGO GPP aligned well with tower GPP across all quantiles, suggested excellent performance for both low and high GPP ranges. Moreover, we conducted a sensitivity experiment by resampling EGO to 0.25° and 0.5°, consistent with X-BASE and FLUXCOM, respectively (Fig. S3). Although its performance declined slightly after resampling ($R^2 = 0.73$ at 0.25° and $R^2 = 0.71$ at 0.5°), EGO still outperformed both products, indicating robustness across spatial scales.

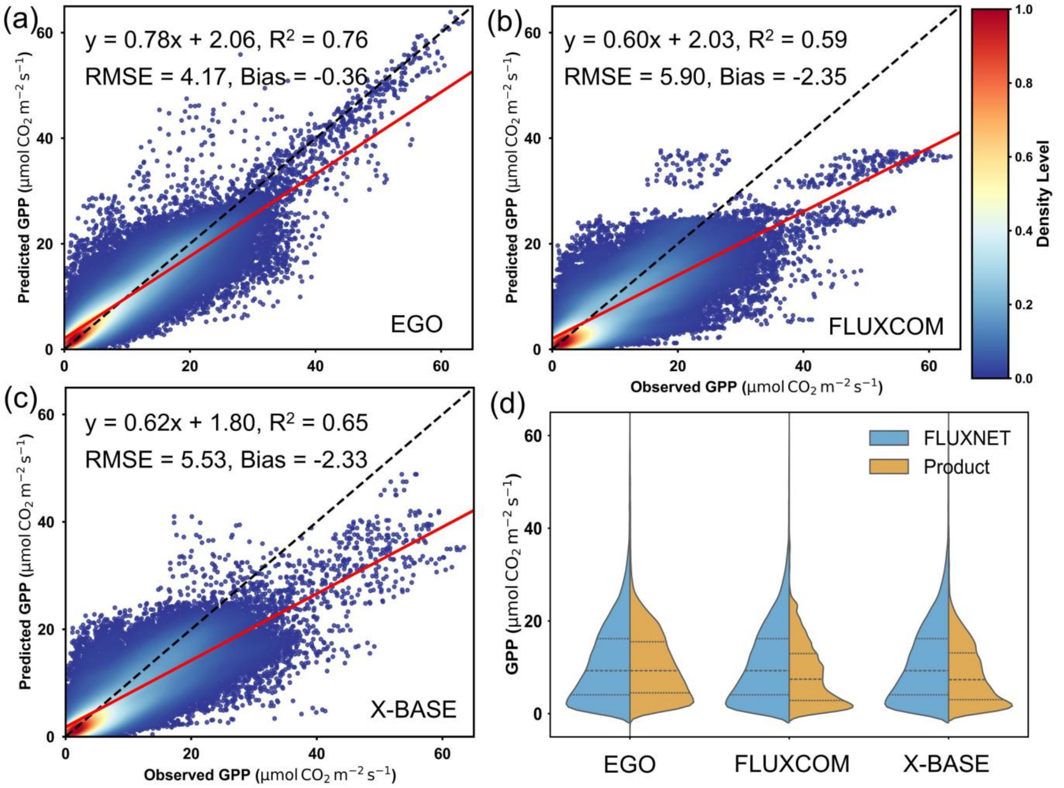

Figure 3. Comparison of the accuracy of EGO GPP and two existing hourly upscaling GPP products. (a-c) represent the predictive performance of EGO, FLUXCOM, and X-BASE, respectively. In each panel, the red solid line and black text indicate the regression line and corresponding performance metrics, while the black dashed line represents the 1:1 reference line. (d) The violin plots illustrate the distributions of tower GPP and products' GPP values—left for the tower and right for the product.

We then applied the SHAP method to interpret feature contributions in CKML-GPP. The results (Fig. 4) showed that SW was the dominant contribution (34.04%), consistent with its role as the primary energy source for vegetation photosynthesis, EVI

(19.54%), Ta (10.03%), LSWI (9.32%), VPD (5.64%), and Aridity (5.33%) were identified as the next most influential drivers, together explaining over 80% of the model's output variance. Among these, SW, EVI, Ta, LSWI and Aridity exerted positive effects on GPP, whereas VPD showed a strong inhibitory effect. Regions dominated by forests and croplands tended to exhibit higher GPP, while areas with larger proportions of grasslands or shrublands showed lower GPP. SHAP interaction analysis (Fig. S4) revealed pronounced synergistic effects among SW, EVI, and LSWI, at a given level of EVI or LSWI, GPP increased substantially with increasing SW, indicating a synergistic coupling among energy supply, canopy structure, and surface moisture in regulating diurnal carbon uptake. In contrast, a strong negative interaction was observed between VPD and Aridity: the suppressive effect of VPD on GPP was more pronounced in drier environments (lower aridity index), implying that ecosystems in drylands are more vulnerable to atmospheric drought.

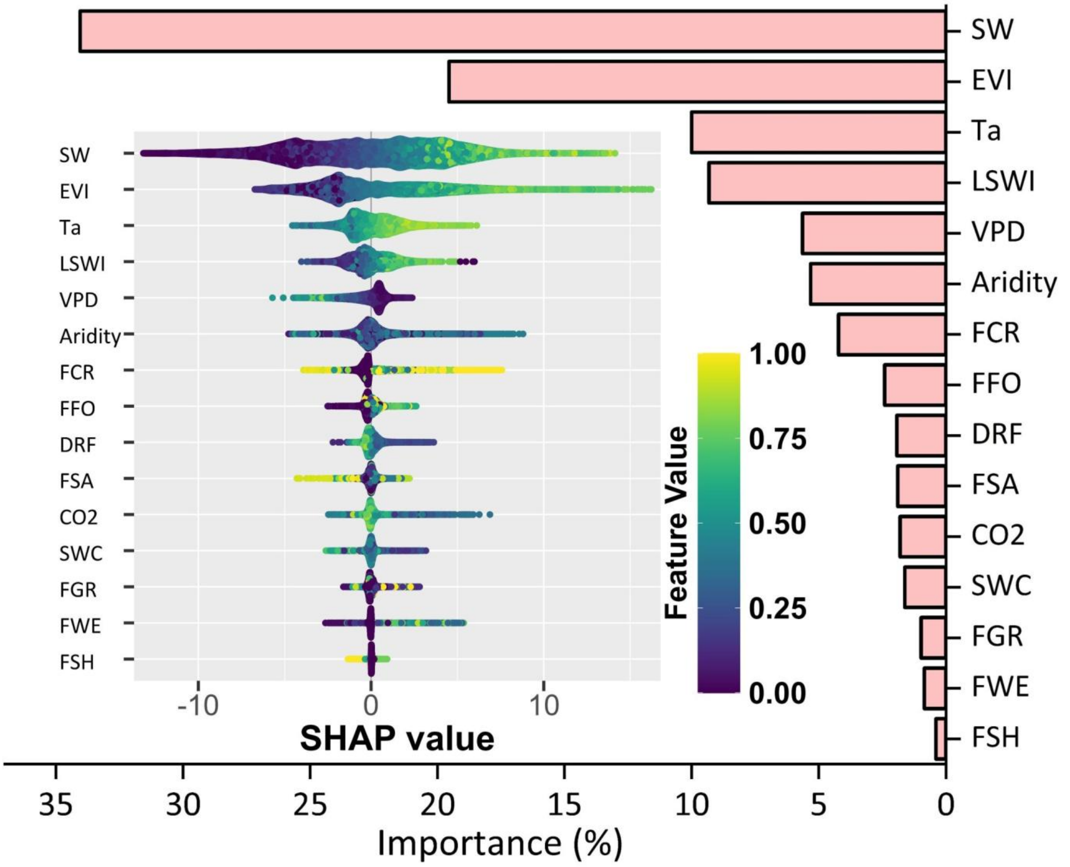

Figure 4. The importance of 15 drivers for hourly GPP modeling. From top to bottom, the importance decreased successively. The subgraph shows the contributions of each driver to hourly GPP. For instance, a high feature value can lead to a positive SHAP value (driver promotes GPP) or a negative SHAP value (driver inhibits GPP). Additionally, we reaffirm the abbreviations each feature: incoming shortwave radiation (SW), enhanced vegetation index (EVI), air temperature (Ta), land surface water index (LSWI), vapor pressure deficit (VPD), aridity index (Aridity), diffuse radiation fraction (DRF), atmospheric CO_2 concentration (CO2) and soil water content (SWC). FCR, FFO, FSA, FGR, FEW, and FSH denoting as the fraction of Cropland, Forest, Savannas, Grassland, Wetland and Shrubland in every 0.05° grid.

We further compared product accuracy across vegetation types and along the aridity gradient. As shown in Fig. 5, EGO GPP consistently outperformed the other products for nearly all vegetation types. For EBF, ENF, and GRA, the R^2 values of EGO GPP all exceeded 0.75. From Fig. 5b, the accuracy of FLUXCOM and X-BASE generally declined markedly with decreasing aridity index. In extremely arid zones (aridity index < 0.2), their R^2 values dropped sharply, indicating that these products struggle to represent photosynthesis in very dry environments. In contrast, EGO GPP maintained relatively high accuracy in these zones ($R^2 > 0.6$), and its performance showed weaker sensitivity to the aridity gradient. To explicitly assess the role of aridity index, we trained additional models with and without aridity index as a predictor (Fig. S5). Incorporating aridity index improved model performance for both the training and test sets, with particularly pronounced gains in drylands. In extremely arid zones, including aridity index increased R^2 by 0.13 for the training set and by 0.08 for the test set (Fig. S6). The largest improvements were found in GRA, SAV, and SHR biomes, which are predominantly distributed in arid and semi-arid regions. These results indicate that aridity index provides complementary information on water availability that is not fully captured by other meteorological or vegetation variables, especially in water-limited ecosystems.

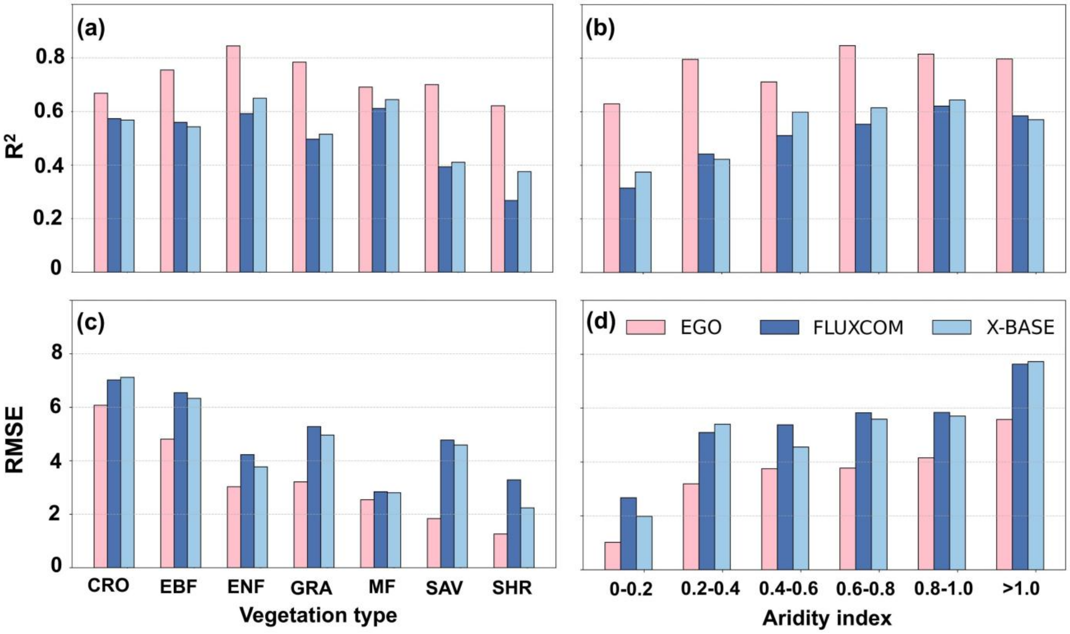

Figure 5. Accuracy comparison of hourly GPP products against tower GPP across different (a, c) vegetation types and (b, d) AI gradients with R^2 shown in (a, b) and RMSE (μmol CO_2 m^{-2} s^{-1}) shown in (c, d).

4.2 Validation of diurnal GPP dynamic

To evaluate the capability of EGO in capturing diurnal photosynthetic variation, we aggregated tower GPP by local solar time within each vegetation type and extracted the corresponding GPP values from each product for comparison. As shown in Fig. 6, EGO showed a clear advantage in reproducing diurnal GPP curve across all vegetation types, whereas FLUXCOM and X-BASE generally underestimated GPP throughout the day. EGO GPP (red line) closely followed the diurnal patterns of tower-based GPP (black line), particularly for NF, CRO, and BF. This advantage extended to water-limited biomes like SAV and

SHR (Fig. 6e and f). In these ecosystems, GPP is not only lower on average but also often peaks before 12:00 due to 360 environmental stress, EGO was the product that mostly accurately captured this earlier peak, aligning closest with the reference curves, while the other products tended to produce lower value and inconsistent diurnal shapes that failed to reflect these patterns. As expected, comparisons at our six selected representative sites across biomes (Fig. S7) further showed that EGO most closely matched FLUXNET observations and effectively captured how diurnal GPP cycles varied across seasons.

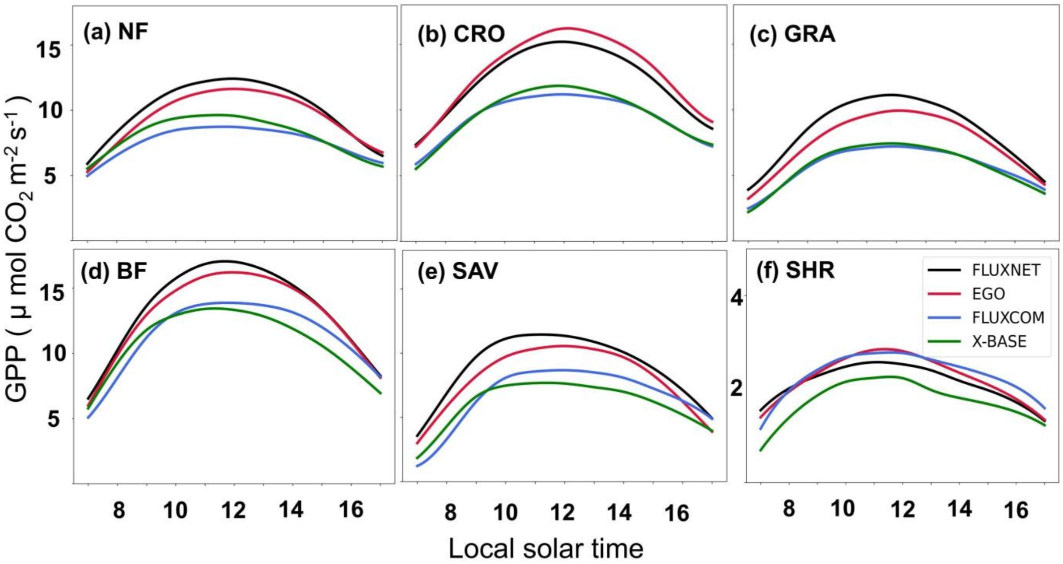

365 **Figure 6.** Mean diurnal GPP cycles for different vegetation types. Each curve represents the averaged diurnal GPP variation during growing seasons across all test sites within the same vegetation category. Observations and product estimates are shown in colors consistent with panel (f). For clarity, vegetation types were moderately aggregated: NF includes evergreen needleleaf forests (ENF) and deciduous needleleaf forests (DNF); BF includes evergreen broadleaf forests (EBF), deciduous broadleaf forests (DBF), and mixed forests (MF).

We further selected six sites with continuous 10-year records for each vegetation type and visualized their diurnal GPP 370 dynamics using fingerprint plots (Fig. 7). These plots simultaneously display hourly variations of tower GPP, EGO GPP, and their differences for each month across multiple years, clearly illustrating the seasonal evolution and the daily progression of photosynthesis from dawn to dusk. For instance, a crop site (CH-Oe2, Fig. 7a) and a forest site (US-Ha1, Fig. 7b) exhibited persistently high photosynthetic activity throughout the daytime, maintaining substantial GPP values nearly year-round, whereas grass site such as US-SRG (Fig. 7d) and shrubland site such as US-Jo1 (Fig. 7e) showed lower GPP levels and 375 pronounced seasonality. Across all sites, EGO GPP demonstrated high consistency with observations, with differences typically below 1 μmol CO_2 m^{-2} s^{-1} at a given time. Importantly, no systematic overestimation or underestimation was apparent in either morning or afternoon periods, indicating its reliability in capturing the overall shape of diurnal GPP curves without introducing temporal bias.

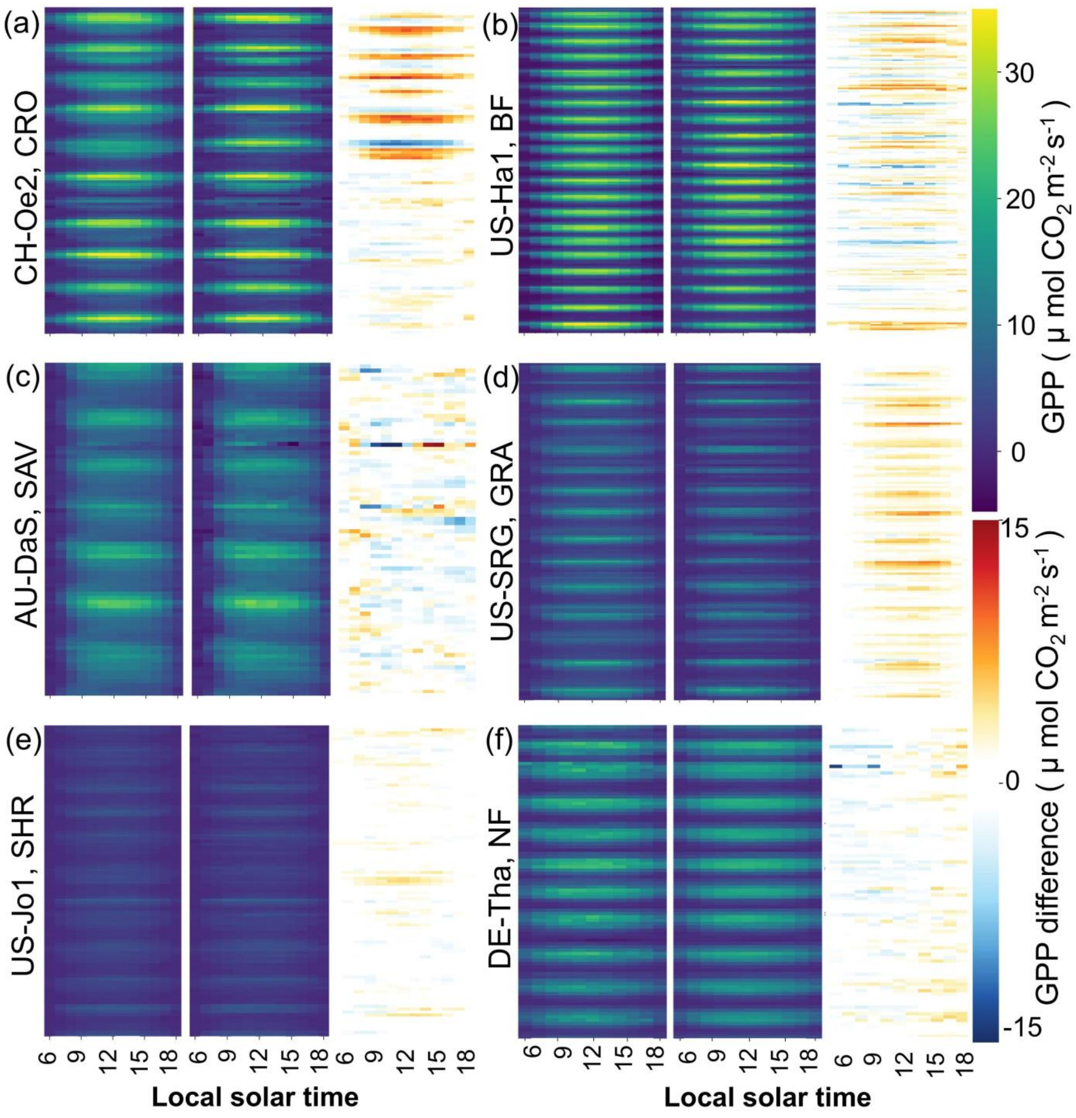

Figure 7. Fingerprint plots of hourly GPP for selected flux tower sites. (a-f) represented the site with the longest observation records across (a) CRO, (b) BF, (c) SAV, (d) GRA, (e) SHR and (f) NF. For each panel, the left plot and the middle plot represented observed and predicted hourly GPP while the right plot was the difference of the two. We manually set the color of legend when value less than 1 to white.

To systematically quantify diurnal GPP patterns, we conducted experiments reconstructing GPP curves by controlling different metric combinations (Text S6). We selected a representative diurnal curve from an arid site (US-Wkg, August 2013) as an example (pink curve in Fig. 8a), which exhibited clear midday depression and pronounced asymmetry (ΔGPP > 0), with both centroid and peak time occurring before noon. When only the absolute magnitude was constrained (Case 1, blue curve), the reconstructed curve deviated substantially from the reference, with both peak and centroid times shifting toward the afternoon. Constraining both magnitude and asymmetry (Case 2, green curve), produced a more realistic curve overall but still failed to reproduce the midday depression. When asymmetry and midday depression were jointly constrained (Case 3, purple curve), the curve shape closely matched the reference, although GPP magnitude was systematically overestimated. In contrast, when all three metrics were jointly constrained (Case 4, yellow curve), the simulated curve nearly overlapped with the reference. These experiments demonstrate that the combined use of mean GPP, ΔGPP and MDI can comprehensively characterize diurnal photosynthetic dynamic.

Under this framework, we constructed a three-dimensional metric space to evaluate how well different products captured diurnal GPP dynamics. In this space (Fig. 8b), a smaller distance between a product and the observed point indicated a more accurate representation of photosynthesis diurnal pattern. Across nearly all vegetation types, EGO GPP was closest to observations. Among the other products, X-BASE performed relatively well in NF and CRO, while FLUXCOM showed better performance in BF and GRA. Overall, EGO not only reproduces the absolute magnitude of GPP but also more accurately captures the diurnal shape of photosynthesis dynamics.

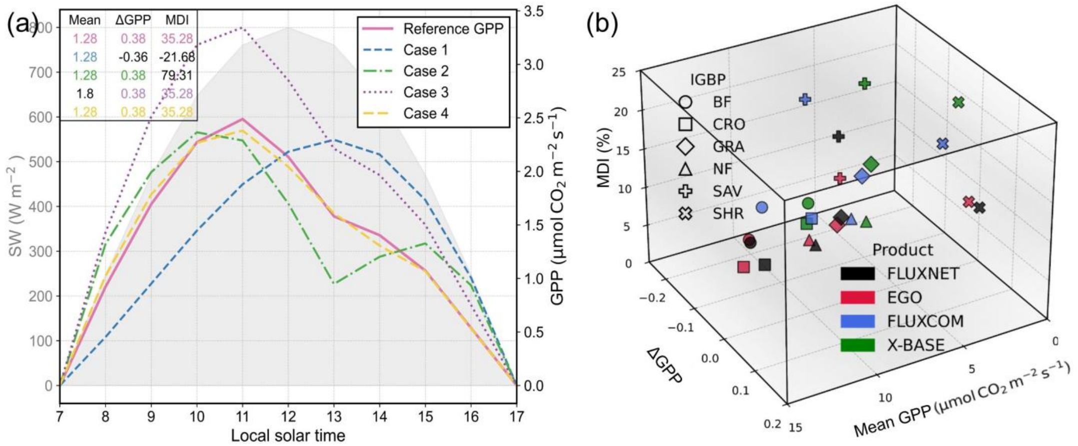

Figure 8. Diurnal GPP pattern evaluation based on diurnal metrics. (a) shows reference GPP and four controlled cases: (1) mean magnitude only, (2) magnitude and asymmetry, (3) asymmetry and midday depression, and (4) all three factors jointly controlled. For each case, a Gaussian-function-based curve generation method were used to produce 100 random diurnal GPP curves satisfying the control conditions, and their mean profiles were shown. (b) presents the performance of products in a three-dimensional metric space, where the X, Y, and Z axes represent Mean GPP (absolute magnitude), ΔGPP (asymmetry), and MDI (midday depression), respectively. Different vegetation types are marked by distinct symbols, and products are distinguished by color. A smaller distance between a product and the observed point in this space indicates a closer match to the observed diurnal GPP dynamics.

4.3 Spatial pattern of global diurnal GPP

We first produced global maps to examine the spatial patterns of EGO GPP at different local solar time (Fig. 9 and Fig. S8). Photosynthesis commenced after sunrise when solar radiation became available. GPP increased throughout the morning (Figs. 9a-c) as light availability improved under favorable temperature and moisture conditions, peaked around noon (Figs. 9d-f), and declined in the afternoon as photosynthetic activity weakened. After sunset, GPP approached zero in the absence of sunlight (Figs. 9g-i). Spatially, regions such as the Amazon, central Africa, and Southeast Asia exhibited consistently high GPP, with midday values exceeding 25 μmol CO_2 m^{-2} s^{-1} at noon. In contrast, high-latitude regions, the western United States, and Australia showed lower photosynthetic activity throughout the day, rarely surpassing 10 μmol CO_2 m^{-2} s^{-1}. Beyond these general patterns, Fig. S9 reveals substantial seasonal variations in diurnal photosynthesis. During June–August, photosynthetic activity intensified across the Northern Hemisphere, with midday GPP exceeding 25 μmol CO_2 m^{-2} s^{-1} in boreal and temperate forests. In December–February, the epicenter of global photosynthetic activity shifted southward, with enhanced photosynthesis in the Southern Hemisphere, particularly in the Amazon and southern Africa. The seasons transition reflects the gradual latitudinal migration of global photosynthesis belt driven by changing light availability. In terms of uncertainty (Fig. S10), the standard deviation of EGO GPP remains below 1 μmol CO_2 m^{-2} s^{-1} across most regions and times, even in high-GPP areas.

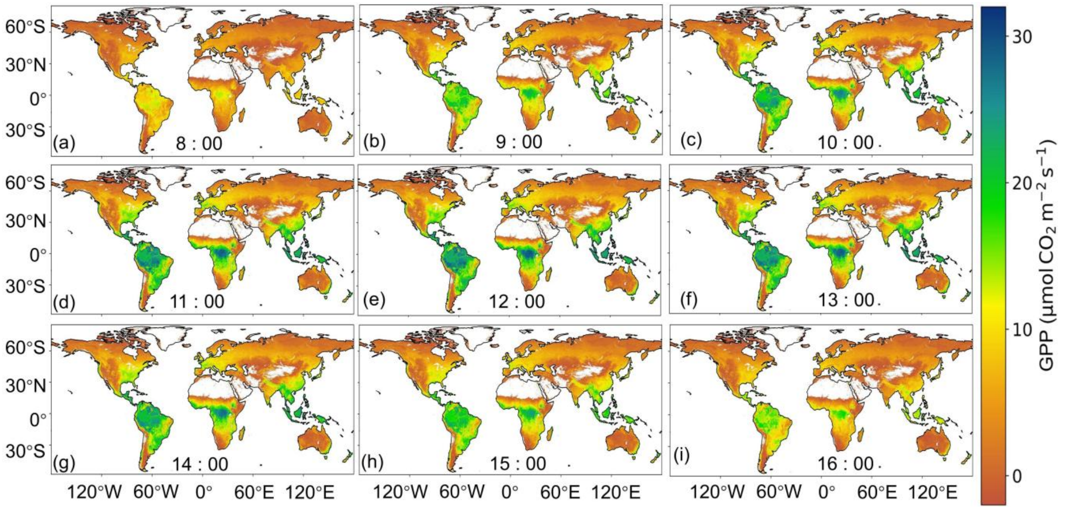

Figure 9. Global diurnal pattern of EGO GPP averaged over the growing seasons from 2000 to 2022, a-i represents the spatial distribution of hourly GPP at 1-hour intervals spanning from 08:00 to 18:00.

Within the selected ROIs, the Amazon represents a core region of strong photosynthetic activity, where EGO and the other products all captured persistently high GPP values (~15 μmol CO_2 m^{-2} s^{-1}) even in the late afternoon (Fig. 10e). Moreover, EGO delineates finer spatial variations within forest types and transition zones, whereas the other products appeared overly smoothed (Fig. 10c, h, and m). This enhanced spatial realism is attributed to the use of sub-grid fractional PFT cover instead of discrete coarse vegetation class labels, which better represents gradual transitions in land cover. Similar advantages in spatial detail are evident in the U.S. (Fig. S11) and Europe (Fig. S12).

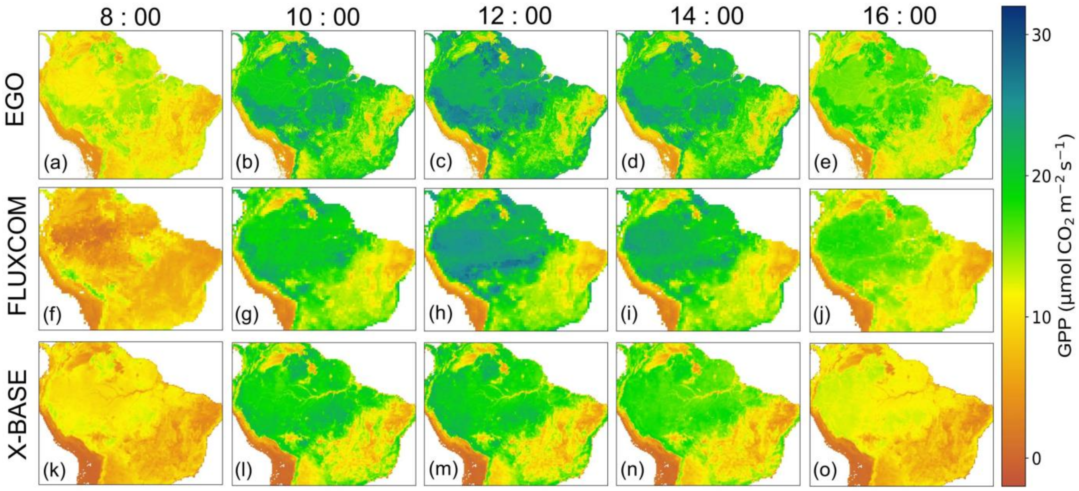

Figure 10. Detailed comparison of diurnal GPP among products in the Amazon. Columns 1-5 show GPP maps from 08:00 to 16:00 at 2 h intervals averaged over the growing seasons from 2000 to 2022, and rows 1-3 correspond to EGO, FLUXCOM, and X-BASE, respectively.

We then presented the multiyear growing-season averages of four diurnal metrics derived from EGO GPP including MDI, ΔGPP, centroid time, and peak time (Fig. 11). Together, these metrics reveal distinct regional characteristics of diurnal photosynthetic dynamics. High MDI values occur mainly in tropical and arid regions, particularly in tropical drylands such as the Somali Peninsula in East Africa, where MDI exceeded 30%. This indicates a pronounced midday depression of photosynthesis, strong physiological downregulation under intense radiation and severe water and heat stress. In contrast, high-latitude vegetation exhibited much weaker midday depression (MDI < 10%) due to lower radiation and more favorable hydrothermal conditions. The spatial patterns of ΔGPP, centroid time, and peak time are strongly consistent. Globally, ΔGPP values are mostly negative, indicating that photosynthetic activity is generally stronger in the afternoon than in the morning. Positive ΔGPP values are concentrated in typical drylands such as the western United States, southern Africa, and Australia, where afternoon photosynthesis was strongly suppressed by water and heat stress. These regions also showed earlier centroid and peak times (before 12:00), associated with rapid morning increases and earlier declines in photosynthetic activity. Conversely, in high-latitude and tropical rainforest regions, ΔGPP is small or negative, and both centroid and peak time occur near or after noon, indicating that photosynthesis remains relatively active in the afternoon.

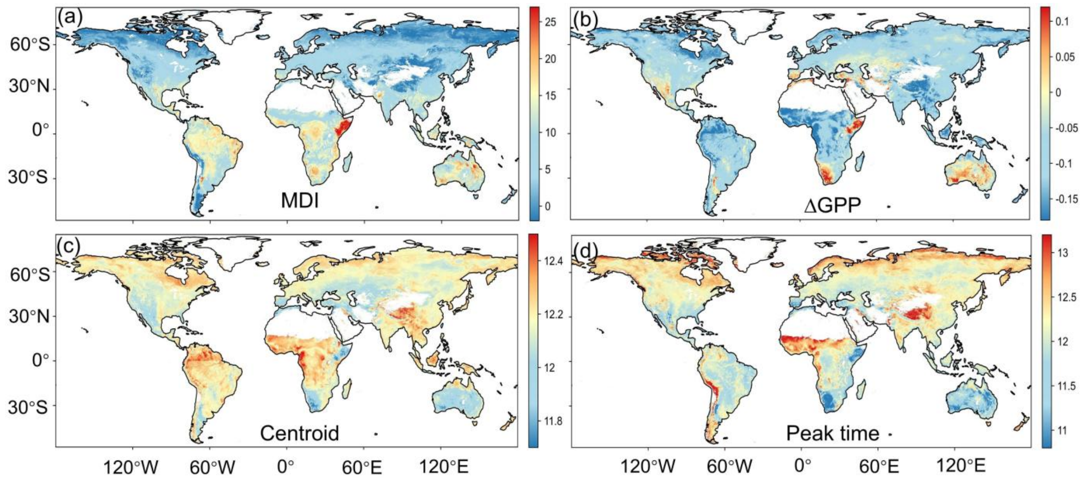

Figure 11. Global map of photosynthetic diurnal metrics derived from EGO GPP averaged over the growing seasons from 2000 to 2022. (a) MDI, (b) ΔGPP, c Centroid, and d Peak time.

4.4 Performance of EGO GPP in capturing the diurnal response of photosynthesis to extreme events

To further assess the performance of EGO GPP under extreme events, we examined two representative cases in the U.S. and Europe and analyzed their impacts on diurnal vegetation photosynthesis. As shown in Fig. 12, vegetation in the northwestern U.S. experienced severe environmental stress in June 2021 relative to the multi-year average: soil moisture decreased by about 40%, while air temperature and VPD increased by approximately 30% and 50%, respectively. Against this backdrop, GPP across most of the U.S. declined markedly, particularly in the western and north-central U.S., where vegetation suffered the strongest stress and GPP losses, approached 50%. In both reference and extreme months, GPP showed a general pattern of lower values in the western U.S. and higher in the east (Fig.S13). We then evaluated EGO's performance using observations from 39 flux towers with valid records during extreme and normal June (Fig. S14a-c). EGO maintained robust performance during the extreme month ($R^2 = 0.69$), comparable to its accuracy in normal Junes ($R^2 = 0.80$). Importantly, EGO effectively captured the GPP anomalies induced by the drought, consistent with ground-based observations ($R^2 = 0.51$).

https://doi.org/10.5194/essd-2026-40
Preprint. Discussion started: 15 April 2026

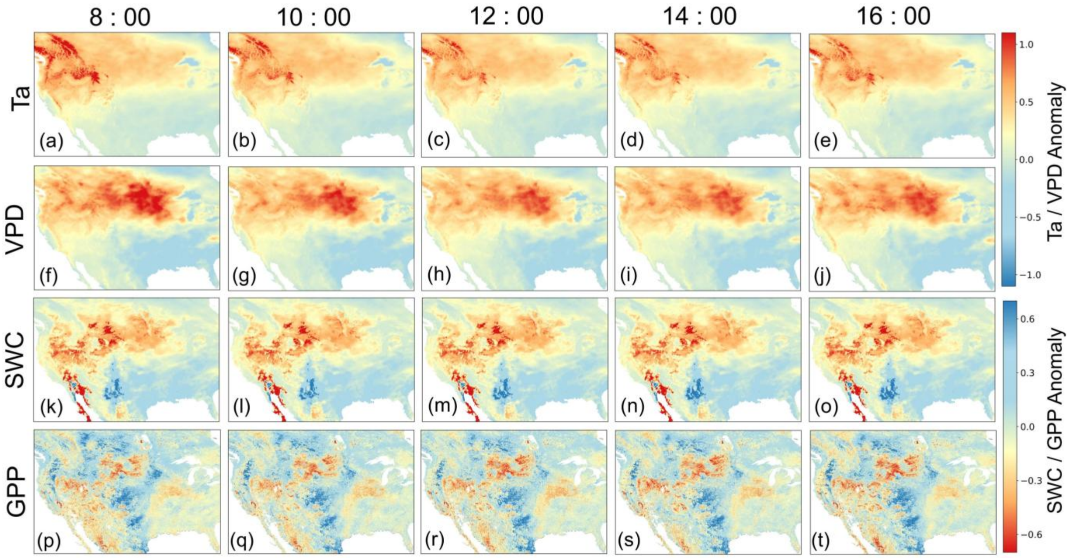

Figure 12. Spatial distribution of (a-e) Ta, (f-j) VPD, (k-o) SWC, and (p-t) GPP anomalies in the U.S. during June 2021. For instance, GPP Anomaly = (GPP_{2021} – GPPreference) / GPPreference.

To further examine diurnal responses, we aggregated observed and EGO GPP across dryland and non-dryland sites in the U.S. In drylands (Fig. 13a), intense water stress in June 2021 (black curve) led to a pronounced shift of the GPP peak, advancing by approximately two hours compared with reference years (gray curve). Consistently, MDI increased from 7.49% to 18.73%, and diurnal asymmetry strengthened (ΔGPP from -0.03 to 0.12). Non-dryland sites (Fig. 13b) showed more moderate changes: overall GPP decreased modestly, while MDI increased from 7.12% to 10.69%, and ΔGPP shifted from -0.04 to 0.02. Across both drylands and non-drylands, EGO GPP closely matched flux-tower observations. More importantly, EGO closely matched flux-tower observations, and successfully reproduced both the direction and magnitude of changes in key diurnal metrics under drought stress.

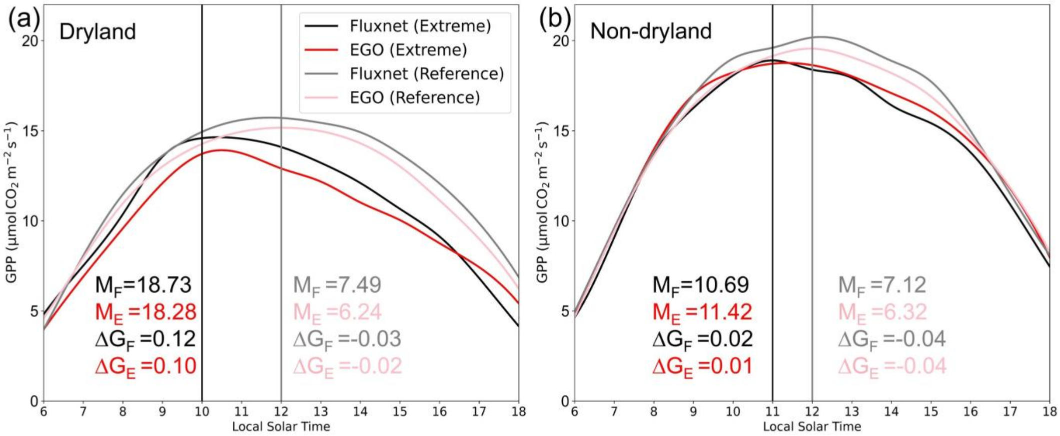

Figure 13. Mean diurnal GPP cycles aggregated for dryland (a) and non-dryland (b) sites in the U.S. Black and red lines denote average GPP cycles for June 2021, while gray and pink lines represent averaged years for June (Reference). The vertical line represents the peak

time. M and ΔG indicate MDI and ΔGPP; F and E denote flux-tower observations and EGO GPP, respectively. Dark and light colors correspond to 2021 and reference-year metrics.

Spatial analyses (Fig. 14) further revealed systematic differences between dryland and non-dryland ecosystems across the U.S. The western U.S., characterized by extensive drylands, exhibited higher MDI and ΔGPP values alongside earlier centroid and peak times (before 12:00) compared to eastern U.S. Under the extreme drought event, these patterns intensified, particularly in the severely affected northwestern U.S., where MDI increased by about 15%, ΔGPP rose by roughly 0.1, the diurnal centroid advanced by nearly 0.2 hours, and peak time shifted earlier by 1 to 2 hours. Strengthening of both midday depression and diurnal asymmetry was more pronounced in drylands than in non-drylands. Diurnal metrics derived from EGO and tower-based GPP (Fig. S15), showed strong agreement for both dryland and non-dryland.

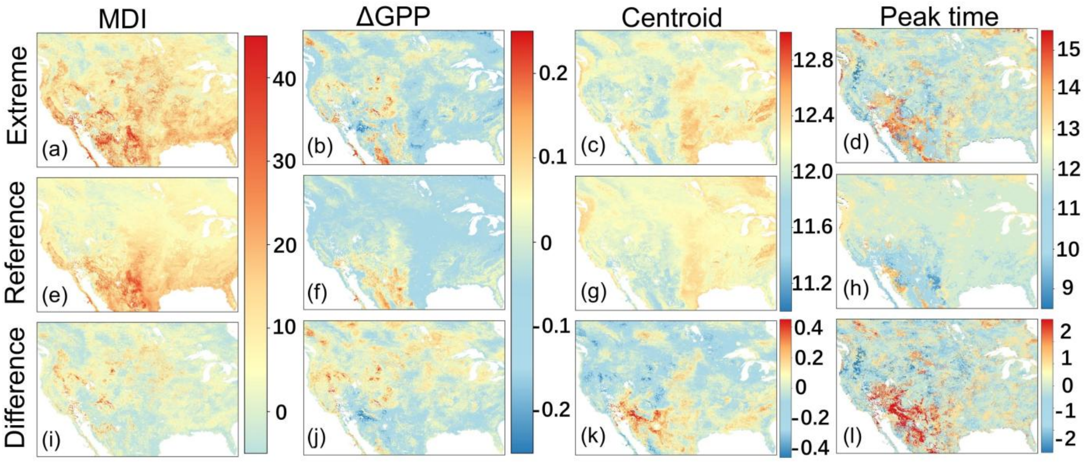

Figure 14. Spatial pattern of the diurnal metrics in the U.S. during extreme (a-d) and averaged reference June (e-h), with (i-l) showing their differences (extreme minus reference).

A similar analysis for the August 2003 European heatwave yielded consistent conclusions. The heatwave caused temperature increases of up to 40% and strongly reduced GPP across all hours, with anomalies reaching about 45% (Fig S16 and Fig S17). The heatwave advanced GPP diurnal peaks by about one hour earlier across Europe, with more pronounced changes in drylands (Fig. S18): MDI increased from 8.26% to 11.33%, and ΔGPP shifted from -0.06 to 0.02. Non-drylands showed gentler responses, with limited changes in morning GPP changes but notable midday depression (MDI up to 10.67%). Although ΔGPP increased across most regions, diurnal asymmetry remained weak outside Mediterranean drylands (Fig. S19), indicating comparatively higher thermal resistance in non-dryland ecosystems. EGO again showed reliable performance during this event, accurately capturing GPP anomalies (R^2= 0.87, RMSE = 1.25%) and associated changes in diurnal metric (Fig. S14d-f & Fig. S20). Taken together, these findings indicate that EGO can reliably characterize the diurnal GPP cycle across a range of hydroclimatic conditions, including both normal and extreme years and both dryland and non-dryland ecosystems, providing a useful dataset for future studies of sub-daily vegetation carbon dynamics.

5 Discussion

5.1 Advantages of EGO GPP

In this study, we developed EGO, a global hourly GPP product generated using a causal knowledge-driven machine learning framework that integrates the PCMCI causal discovery algorithm with an XGBoost model. EGO demonstrated strong performance across multiple dimensions: it achieved high accuracy in simulating tower-based hourly GPP (Section 4.1) and reconstructing diurnal GPP curves (Section 4.2), reliably characterized diurnal GPP dynamic at the global scale (Section 4.3), and accurately captured photosynthetic diurnal responses under extreme drought and heatwave events (Section 4.4). The robust performance of EGO GPP stems from several advances in both model architecture and input variables.

Firstly, EGO employs a semi-empirical modelling framework based on PCMCI-XGBoost model, enabling strong nonlinear representation while explicitly accounting for causal effect of predictor variables on GPP (Garcia-Leon et al., 2021). Identifying robust causal structures is critical for data-driven machine learning, as the magnitude of hourly GPP response to environmental changes strongly depends on the strength of specific causal effects rather than mere statistical correlations (Galytska et al., 2023; Krich et al., 2020; Yuan et al., 2022). It has been successfully demonstrated in other complex ecological tasks, such as estimating wetland methane emissions (Yuan et al., 2024) and ecosystem respiration (Zhao et al., 2025; Zhao and Zhu, 2025). The superior performance observed in our evaluations also confirms the effectiveness of this causal modelling framework. Secondly, EGO integrates multidimensional predictors encompassing vegetation, radiation, both long-term and short-term water availability, and land-use dynamics, thereby allowing the model to fully learn the drivers of the diurnal GPP cycle (Anav et al., 2015; Hou et al., 2022; Pei et al., 2025; Wang et al., 2023). Unlike previous products that primarily relied on short-term water variability predictors, EGO explicitly introduced the aridity index as a proxy for long-term climatic water balance which plays a pivotal role in regulating the diurnal hysteresis (Li et al., 2023; Liu et al., 2024). As shown in Fig. S6, incorporating aridity index as a predictor substantially improved hourly GPP simulation accuracy especially in drylands. This improvement directly mitigates the uncertainties of existing products in arid regions. Thirdly, we used sub-pixel vegetation endmember abundance data rather than discrete vegetation type as model inputs. Traditional machine learning upscaling often assigns a single dominant vegetation class to each pixel, which neglects surface heterogeneity and introduces mixed-pixel bias (Bodesheim et al., 2018; Nelson et al., 2024). By contrast, the endmember abundances enable EGO to resolve continuous transitions among vegetation types and capture detailed local variations in photosynthesis (Qin et al., 2023). Finally, EGO adopted a 10-fold cross-validation ensemble strategy, where predictions from all folds were averaged to produce the final GPP output. This ensemble integration not only stabilized the learning process against random sample partitioning but also improved generalization by aggregating information learned from diverse training subsets (Han et al., 2025; Kang et al., 2025). Consequently, the ensemble output demonstrated higher accuracy than any single-fold model and reduced the influence of potential overfitting. To our knowledge, EGO represents the highest spatial resolution (0.05°) global hourly GPP product currently available, may extends the potential applicability for addressing localized ecological questions and refining global carbon budget assessments. Together, these advances in modelling strategy and data integration underpin the strong performance of EGO GPP and its capability to reproduce sub-daily vegetation carbon dynamics across biomes and climatic conditions.

5.2 Implications for future research

We developed quantitative metrics to characterize the morphology of GPP diurnal cycles, describing the curves in terms of absolute magnitude, asymmetry, and midday depression. Beyond providing site-scale diagnostics, we mapped the global distributions of these metrics and analyzed their variations under extreme drought and heatwave events, thereby offering a holistic perspective for assessing how vegetation photosynthesis responds to environmental perturbations. This framework offers a new analytical perspective for evaluating hourly GPP products, shifting the focus beyond traditional accuracy performance to diurnal dynamics.

Previous studies on diurnal photosynthetic dynamics have mostly been confined to regional or site scales (Lin et al., 2019; Zhu and Zhu, 2025). Our earlier study reported that the 2020 U.S. heatwave substantially altered diurnal GPP patterns especially in western dryland ecosystems, causing widespread afternoon depression and earlier diurnal centroids (Li et al., 2023). Zhang et al. (2023) used OCO-3 and tower observations to reveal distinct morning-afternoon responses of Amazon forests to atmospheric warming and drying, where enhanced morning photosynthesis partially compensated for afternoon declines driven by high VPD. Xiao et al. (2021) combined Himawari-8 AHI with tower observations to demonstrate substantial afternoon GPP reductions during Australian heatwaves. These findings collectively highlight that vegetation can rapidly adjust to short-term environmental stresses through physiological processes such as stomatal regulation and photoprotective mechanisms which cannot be adequately captured by traditional daily or monthly GPP data (Novick et al., 2024; Li et al., 2025; Xiao et al., 2025). With the increase in the frequency of extreme climate events, midday and afternoon depression of photosynthesis may intensify globally, underscoring the need for high-resolution GPP products capable of resolving these fine-scale dynamics (Li et al., 2023; Zhang et al., 2023). Our systematic evaluation confirms EGO's capability in this regard. During the two representative extreme events in this study (2021 U.S. drought and the 2003 European heatwave), EGO accurately captured stress-induced changes in diurnal metrics, including widespread GPP reductions, earlier peaks and centroids, and intensified asymmetry and midday depression.

Given these strengths, EGO GPP holds strong potential as a reliable data source for investigating global diurnal photosynthesis and exploring ecosystem dynamics under extreme stresses in future research. Moreover, EGO can serve as a valuable benchmark for Earth system models, supporting the development and evaluation of next-generation carbon cycle simulations at hourly time steps (Boucher et al., 2020; Liu et al., 2024; Seferian et al., 2019; Voldoire et al., 2019). We will continue to update and distribute EGO to facilitate advanced understanding of global vegetation dynamics in a changing world.

5.3 Uncertainties and limitations

Although EGO demonstrated robust performance, several limitations remain. Due to the uneven spatial distribution of global flux sites, most observations were concentrated in Europe and America (Fig. 1). As a result, the model is trained primarily on these regions, which may introduce bias at the global scale (Bodesheim et al., 2018; Nelson et al., 2024). While this is a prevalent issue in current studies, we anticipate that these uncertainties will be progressively alleviated by the continuous expansion of flux observation networks and strengthened international collaboration on data sharing (Xiao et al., 2025). Moreover, we used MERRA-2 (0.5°× 0.625°) and CarbonTracker (3° × 2°) datasets to represent the effects of diffuse radiation fraction and atmospheric CO_2 concentration on diurnal GPP dynamics. Their spatial resolutions are coarser than the EGO's 0.05° grid, some spatial detail may have been smoothed, especially in heterogeneous landscapes. Also, the intrinsic uncertainties associated with these reanalysis products may propagate into the model, ultimately affecting GPP estimating accuracy (Wang, 2026). Nevertheless, to our knowledge, these datasets were currently the good available sources that provide hourly variable, thus remain a reasonable compromise that balance data quality and feasibility. In addition, potential uncertainties may arise in mountainous regions. In complex terrain, topographic effects on solar radiation and satellite observation geometry are difficult to fully correct, potentially impacting model performance (Cao et al., 2025; Hao et al., 2022). Since we used MCD12Q1 product, the model cannot capture GPP variations caused by intra-annual land use transitions (e.g., seasonal deforestation or crop rotation) that occur within a single year. Finally, limited by computational resources and data processing efficiency, the released EGO GPP was currently provided as monthly-averaged hourly data. Despite this, EGO is sufficient to support a wide range of studies focusing on diurnal photosynthesis dynamics. Looking ahead, our roadmap includes leveraging advanced cloud computing to produce a daily-hourly product, which will significantly enhance the capability to resolve short-term ecosystem processes.

6 Conclusion

We developed a global hourly GPP product (EGO GPP) with 0.05° spatial resolution from 2000 to 2022, based on a causal knowledge-driven machine learning model. By integrating multi-dimensional predictors including meteorological variables, vegetation properties, and indicators of both short-term and long-term water availability, EGO GPP effectively captures diurnal vegetation photosynthetic processes. We systematically evaluated the product's performance through three aspects: overall accuracy, representation of diurnal cycles, and spatiotemporal patterns. Results confirmed that EGO GPP exhibits robust capabilities across all these dimensions. Furthermore, through case studies of two extreme climate events, we demonstrated EGO's ability to reliably capture drought- and heatwave-induced changes in diurnal photosynthesis. In summary, EGO GPP provides a reliable data foundation for advancing our understanding of global diurnal vegetation photosynthesis and its complex interactions with the environment.

Data availability and code availability

EGO GPP and related codes is publicly available on the Zenodo platform through https://doi.org/10.5281/zenodo.18253238 (Liu et al., 2026). It has a spatial resolution of 0.05° and covers the period 2000–2022 with monthly-averaged GPP for each hour between 6:00 to 18:00 of local solar time. It is important to note that, like other machine learning-based GPP products, EGO may occasionally yield slightly negative GPP estimates, particularly under very low light conditions. Rather than truncating these values, we retained them in the published dataset to avoid introducing systematic bias. Users can easily apply a zero-threshold filter based on their specific application needs. The hourly GPP was stored in NetCDF4 format and their units consistent with FLUXNET (μmol CO_2 m^{-2} s^{-1}). Moreover, users must apply a conversion factor of 0.001 to retrieve the actual values. To facilitate user accessibility and interoperability, we also provided a Python script for converting NetCDF4 files to GeoTIFF format.

Author contributions

Xing Li and Xi Liu designed the experiments, and Xi Liu carried them out. Xi Liu, Yanan Zhou and Cenliang Zhao developed the model code and performed the simulations. Xi Liu prepared the original draft and all the co-authors review and editing them.

Competing interests

At least one of the (co-)authors is a member of the editorial board of Earth System Science Data. The authors have no other competing interests to declare.

Acknowledgements

We are grateful to the FLUXNET and AmeriFlux communities for providing eddy covariance flux observations. We also thank the teams associated with the data sources listed in Table S2 for their valuable contributions. In particular, we thank Prof. Paul Bodesheim for providing the FLUXCOM dataset (https://doi.org/10.17871/BACI.224) and Prof. Jacob A. Nelson for providing the X-BASE dataset (https://doi.org/10.5194/bg-21-5079-2024).

Financial support

This work was supported by the National Natural Science Foundation of China (Grant number 42401412).

References

Anav, A., Friedlingstein, P., Beer, C., Ciais, P., Harper, A., Jones, C., Murray-Tortarolo, G., Papale, D., Parazoo, N. C., Peylin, P., Piao, S., Sitch, S., Viovy, N., Wiltshire, A., and Zhao, M.: Spatiotemporal patterns of terrestrial gross primary production : a review, Rev. Geophys., 53, 785-818, https://doi.org/10.1002/2015RG000483, 2015.

Beer, C., Reichstein, M., Tomelleri, E., Ciais, P., Jung, M., Carvalhais, N., Roedenbeck, C., Arain, M. A., Baldocchi, D., Bonan, G. B., Bondeau, A., Cescatti, A., Lasslop, G., Lindroth, A., Lomas, M., Luyssaert, S., Margolis, H., Oleson, K. W., Roupsard, O., Veenendaal, E., Viovy, N., Williams, C., Woodward, F. I., and Papale, D.: Terrestrial gross carbon dioxide uptake: global distribution and covariation with climate, Science, 329, 834-838, https://doi.org/10.1126/science.1184984, 2010.

Bodesheim, P., Jung, M., Gans, F., Mahecha, M. D., and Reichstein, M.: Upscaled diurnal cycles of land-atmosphere fluxes : a new global half-hourly data product, Earth Syst. Sci. Data, 10, 1327-1365, https://doi.org/10.5194/essd-10-1327-2018, 2018.

Boucher, O., Servonnat, J., Albright, A. L., Aumont, O., Balkanski, Y., Bastrikov, V., Bekki, S., Bonnet, R., Bony, S., Bopp, L., Braconnot, P., Brockmann, P., Cadule, P., Caubel, A., Cheruy, F., Codron, F., Cozic, A., Cugnet, D., D'Andrea, F., Davini, P., de Lavergne, C., Denvil, S., Deshayes, J., Devilliers, M., Ducharne, A., Dufresne, J., Dupont, E., Ethe, C., Fairhead, L., Falletti, L., Flavoni, S., Foujols, M., Gardoll, S., Gastineau, G., Ghattas, J., Grandpeix, J., Guenet, B., Guez, L. E., Guilyardi, E., Guimberteau, M., Hauglustaine, D., Hourdin, F., Idelkadi, A., Joussaume, S., Kageyama, M., Khodri, M., Krinner, G., Lebas, N., Levavasseur, G., Levy, C., Li, L., Lott, F., Lurton, T., Luyssaert, S., Madec, G., Madeleine, J., Maignan, F., Marchand, M., Marti, O., Mellul, L., Meurdesoif, Y., Mignot, J., Musat, I., Ottle, C., Peylin, P., Planton, Y., Polcher, J., Rio, C., Rochetin, N., Rousset, C., Sepulchre, P., Sima, A., Swingedouw, D., Thieblemont, R., Traore, A. K., Vancoppenolle, M., Vial, J., Vialard, J., Viovy, N., and Vuichard, N.: Presentation and evaluation of the IPSL-CM6a-LR climate model, J. Adv. Model. Earth Syst., 12, 52, https://doi.org/10.1029/2019MS002010, 2020.

Cao, J., Wang, R., Chen, J. M., Yang, M., Cheng, Z., and Miao, G.: Quantifying topographic effects on carbon and water fluxes over mountainous areas, J. Geophys. Res.-Biogeosci., 130, 20, https://doi.org/10.1029/2025JG008878, 2025.

Chen, H. W., Zhang, L. N., Zhang, F., Davis, K. J., Lauvaux, T., Pal, S., Gaudet, B., and Digangi, J. P.: Evaluation of regional CO 2 mole fractions in the ECMWF CAMS real-time atmospheric analysis and NOAA CarbonTracker near-real-time reanalysis with airborne observations from ACT-america field campaigns, J. Geophys. Res.-Atmos., 124, 8119-8133, https://doi.org/10.1029/2018JD029992, 2019.

Chu, H., Christianson, D. S., Cheah, Y., Pastorello, G., O'Brien, F., Geden, J., Ngo, S., Hollowgrass, R., Leibowitz, K., Beekwilder, N. F., Sandesh, M., Dengel, S., Chan, S. W., Santos, A., Delwiche, K., Yi, K., Buechner, C., Baldocchi, D., Papale, D., Keenan, T. F., Biraud, S. C., Agarwal, D. A., and Torn, M. S.: AmeriFlux BASE data pipeline to support network growth and data sharing, Sci. Data, 10, 13, https://doi.org/10.1038/s41597-023-02531-2, 2023.

Deng, Z., Chen, J., Wang, S., Li, T., Huang, K., Gu, P., Peng, H., and Chen, Z.: Response of vegetation photosynthesis to the 2022 drought in yangtze river basin by diurnal orbiting carbon observatory-2/3 satellite observations, Journal of Remote Sensing, 5, 19, https://doi.org/10.34133/remotesensing.0445, 2025.

Galytska, E., Weigel, K., Handorf, D., Jaiser, R., Koehler, R., Runge, J., and Eyring, V.: Evaluating causal arctic-midlatitude teleconnections in CMIP6, J. Geophys. Res.-Atmos., 128, 25, https://doi.org/10.1029/2022JD037978, 2023.

Garcia-Leon, D., Casanueva, A., Standardi, G., Burgstall, A., Flouris, A. D., and Nybo, L.: Current and projected regional economic impacts of heatwaves in europe, Nat. Commun., 12, 10, https://doi.org/10.1038/s41467-021-26050-z, 2021.

Han, Q., Zeng, Y., Wang, Y., Alidoost, F., Nattino, F., Liu, Y., and Su, B.: FluxHourly: global long-term hourly 9 km terrestrial water-energy-carbon fluxes, Earth Syst. Sci. Data, 17, 7101-7117, https://doi.org/10.5194/essd-17-7101-2025, 2025.

Hao, D., Bisht, G., Huang, M., Ma, P., Tesfa, T., Lee, W., Gu, Y., and Leung, L. R.: Impacts of sub-grid topographic representations on surface energy balance and boundary conditions in the e3SM land model: a case study in sierra nevada, J. Adv. Model. Earth Syst., 14, 21, https://doi.org/10.1029/2021MS002862, 2022.

Hou, H., Zhou, B., Pei, F., Hu, G., Su, Z., Zeng, Y., Zhang, H., Gao, Y., Luo, M., and Li, X.: Future land use/land cover change has nontrivial and potentially dominant impact on global gross primary productivity, Earth Future, 10, 20, https://doi.org/10.1029/2021EF002628, 2022.

Huete, A., Didan, K., Miura, T., Rodriguez, E. P., Gao, X., and Ferreira, L. G.: Overview of the radiometric and biophysical performance of the MODIS vegetation indices, Remote Sens. Environ., 83, 195-213, https://doi.org/DOI 10.1016/S0034-4257(02)00096-2, 2002.

Ichii, K., Ueyama, M., Kondo, M., Saigusa, N., Kim, J., Alberto, M. C., Ardoe, J., Euskirchen, E. S., Kang, M., Hirano, T., Joiner, J., Kobayashi, H., Marchesini, L. B., Merbold, L., Miyata, A., Saitoh, T. M., Takagi, K., Varlagin, A., Bret-Harte, M. S., Kitamura, K., Kosugi, Y., Kotani, A., Kumar, K., Li, S., Machimura, T., Matsuura, Y., Mizoguchi, Y., Ohta, T., Mukherjee, S., Yanagi, Y., Yasuda, Y., Zhang, Y., and Zhao, F.: New data-driven estimation of terrestrial CO 2 fluxes in asia using a standardized database of eddy covariance measurements, remote sensing data, and support vector regression, J. Geophys. Res.-Biogeosci., 122, 767-795, https://doi.org/10.1002/2016JG003640, 2017.

Ishaque, K. and Salam, Z.: A deterministic particle swarm optimization maximum power point tracker for photovoltaic system under partial shading condition, IEEE Trans. Ind. Electron., 60, 3195-3206, https://doi.org/10.1109/TIE.2012.2200223, 2013.

Jeong, S., Ryu, Y., Dechant, B., Li, X., Kong, J., Choi, W., Kang, M., Yeom, J., Lim, J., Jang, K., and Chun, J.: Tracking diurnal to seasonal variations of gross primary productivity using a geostationary satellite , GK-2a advanced meteorological imager, Remote Sens. Environ., 284, 16, https://doi.org/10.1016/j.rse.2022.113365, 2023.

Jiang, Y., Smerdon, J. E., Seager, R., Wang, G., Cook, B. I., Zheng, C., Mankin, J. S., and Williams, A. P.: The influence of land-surface conditions on the 2020-2021 western US drought, Water Resour. Res., 61, 21, https://doi.org/10.1029/2024WR038124, 2025.

Kang, Y., Bassiouni, M., Gaber, M., Lu, X., and Keenan, T. F.: CEDAR-GPP: spatiotemporally upscaled estimates of gross primary productivity incorporating CO 2 fertilization, Earth Syst. Sci. Data, 17, 3009-3046, https://doi.org/10.5194/essd-17-3009-2025, 2025.

Koppa, A., Keune, J., Schumacher, D. L., Michaelides, K., Singer, M., Seneviratne, S. I., and Miralles, D. G.: Dryland self-expansion enabled by land-atmosphere feedbacks, Science, 385, 967-972, https://doi.org/10.1126/science.adn6833, 2024.

Kretschmer, M., Adams, S., Arribas, A., Prudden, R., Robinson, N., Saggioro, E., and Shepherd, T. G.: Quantifying causal pathways of teleconnections, Bull. Amer. Meteorol. Soc., 102, E2247-E2263, https://doi.org/10.1175/BAMS-D-20-0117.1, 2021.

Krich, C., Runge, J., Miralles, D. G., Migliavacca, M., Perez-Priego, O., El-Madany, T., Carrara, A., and Mahecha, M. D.: Estimating causal networks in biosphere - atmosphere interaction with the PCMCI approach, Biogeosciences, 17, 1033-1061, https://doi.org/10.5194/bg-17-1033-2020, 2020.

Kursa, M. B. and Rudnicki, W. R.: Feature selection with the boruta package, J. Stat. Softw., 36, 1-13, https://doi.org/DOI 10.18637/jss.v036.i11, 2010.

Leng, J., Chen, J. M., Li, W., Luo, X., Xu, M., Liu, J., Wang, R., Rogers, C., Li, B., and Yan, Y.: Global datasets of hourly carbon and water fluxes simulated using a satellite-based process model with dynamic parameterizations, Earth Syst. Sci. Data, 16, 1283-1300, https://doi.org/10.5194/essd-16-1283-2024, 2024.

Li, Q., Chen, X., Yuan, W., Lu, H., Shen, R., Wu, S., Gong, F., Dai, Y., Liu, L., Sun, Q., Zhang, C., and Su, Y.: Remote sensing of seasonal climatic constraints on leaf phenology across pantropical evergreen forest biome, Earth Future, 9, 18, https://doi.org/10.1029/2021EF002160, 2021.

Li, W., Yao, Z., Qu, Y., Yang, H., Song, Y., Song, L., Wu, L., and Cui, Y.: A benchmark dataset for global evapotranspiration estimation based on FLUXNET2015 from 2000 to 2022, Earth Syst. Sci. Data, 17, 3835-3855, https://doi.org/10.5194/essd-17-3835-2025, 2025.

Li, X., Ryu, Y., Xiao, J., Dechant, B., Liu, J., Li, B., Jeong, S., and Gentine, P.: New-generation geostationary satellite reveals widespread midday depression in dryland photosynthesis during 2020 western US heatwave, Sci. Adv., 9, 14, https://doi.org/10.1126/sciadv.adi0775, 2023.

Li, X., Zhao, L., Zhang, T., Zhang, Z., and Fu, S.: Assessing the impacts of dry-heat extremes on grassland gross primary productivity across mainland china using multi-source remote sensing data, Information Geography, 2, 100038, https://doi.org/10.1016/j.infgeo.2025.100038, 2026.

Lin, C., Gentine, P., Frankenberg, C., Zhou, S., Kennedy, D., and Li, X.: Evaluation and mechanism exploration of the diurnal hysteresis of ecosystem fluxes, Agric. For. Meteorol., 278, 14, https://doi.org/10.1016/j.agrformet.2019.107642, 2019.

Liu, J., Wang, Q., Zhan, W., Lian, X., and Gentine, P.: When and where soil dryness matters to ecosystem photosynthesis, Nat. Plants, 11, 23, https://doi.org/10.1038/s41477-025-02024-7, 2025.

Xi, L., & Xing, L. (2026). EGO: a global 0.05° hourly GPP dataset for monitoring diurnal photosynthesis dynamics [Data set]. Zenodo. https://doi.org/10.5281/zenodo.18253238.

Liu, Y., Penuelas, J., Cescatti, A., Zhang, Y., and Zhang, Z.: Atmospheric dryness dominates afternoon depression of global terrestrial photosynthesis, Geophys. Res. Lett., 51, 12, https://doi.org/10.1029/2024GL110954, 2024.

Liu, Y., Zhao, D., Zhang, Y., and Zhang, Z.: Global 0.1-degree monthly mean hourly total canopy solar-induced chlorophyll fluorescence dataset derived from random forest, Remote Sens., 17, 24, https://doi.org/10.3390/rs17203429, 2025.

Munoz-Sabater, J., Dutra, E., Agusti-Panareda, A., Albergel, C., Arduini, G., Balsamo, G., Boussetta, S., Choulga, M., Harrigan, S., Hersbach, H., Martens, B., Miralles, D. G., Piles, M., Rodriguez-Fernandez, N. J., Zsoter, E., Buontempo, C., and Thepaut, J.: ERA5-land: a state-of-the-art global reanalysis dataset for land applications, Earth Syst. Sci. Data, 13, 4349-4383, https://doi.org/10.5194/essd-13-4349-2021, 2021.

Nathaniel, J., Liu, J., and Gentine, P.: MetaFlux: meta-learning global carbon fluxes from sparse spatiotemporal observations, Sci. Data, 10, 15, https://doi.org/10.1038/s41597-023-02349-y, 2023.

Nelson, J. A., Carvalhais, N., Migliavacca, M., Reichstein, M., and Jung, M.: Water-stress-induced breakdown of carbon - water relations : indicators from diurnal FLUXNET patterns, Biogeosciences, 15, 2433-2447, https://doi.org/10.5194/bg-15-2433-2018, 2018.

Nelson, J. A., Walther, S., Gans, F., Kraft, B., Weber, U., Novick, K., Buchmann, N., Migliavacca, M., Wohlfahrt, G., Sigut, L., Ibrom, A., Papale, D., Gockede, M., Duveiller, G., Knohl, A., Hortnagl, L., Scott, R. L., Zhang, W., Hamdi, Z. M., Reichstein, M., Aranda-Barranco, S., Ardo, J., de Beeck, M. O., Billesbach, D., Bowling, D., Bracho, R., Brummer, C., Camps-Valls, G., Chen, S., Cleverly, J. R., Desai, A., Dong, G., El-Madany, T. S., Euskirchen, E. S., Feigenwinter, I., Galvagno, M., Gerosa, G. A., Gielen, B., Goded, I., Goslee, S., Gough, C. M., Heinesch, B., Ichii, K., Jackowicz-Korczynski, M. A., Klosterhalfen, A., Knox, S., Kobayashi, H., Kohonen, K., Korkiakoski, M., Mammarella, I., Gharun, M., Marzuoli, R., Matamala, R., Metzger, S., Montagnani, L., Nicolini, G., O'Halloran, T., Ourcival, J., Peichl, M., Pendall, E., Reverter, B. R., Roland, M., Sabbatini, S., Sachs, T., Schmidt, M., Schwalm, C. R., Shekhar, A., Silberstein, R., Silveira, M. L., Spano, D., Tagesson, T., Tramontana, G., Trotta, C., Turco, F., Vesala, T., Vincke, C., Vitale, D., Vivoni, E. R., Wang, Y., Woodgate, W., Yepez, E. A., Zhang, J., Zona, D., and Jung, M.: X-BASE: the first terrestrial carbon and water flux products from an extended data-driven scaling framework , FLUXCOM-x, Biogeosciences, 21, 5079-5115, https://doi.org/10.5194/bg-21-5079-2024, 2024.

Novick, K. A., Ficklin, D. L., Grossiord, C., Konings, A. G., Martinez-Vilalta, J., Sadok, W., Trugman, A. T., Williams, A. P., Wright, A. J., Abatzoglou, J. T., Dannenberg, M. P., Gentine, P., Guan, K., Johnston, M. R., Lowman, L. E. L., Moore, D. J. P., and Mcdowell, N. G.: The impacts of rising vapour pressure deficit in natural and managed ecosystems, Plant Cell Environ., 47, 3561-3589, https://doi.org/10.1111/pce.14846, 2024.

Pastorello, G., Trotta, C., Canfora, E., Chu, H., Christianson, D., Cheah, Y., Poindexter, C., Chen, J., Elbashandy, A., Humphrey, M., Isaac, P., Polidori, D., Ribeca, A., van Ingen, C., Zhang, L., Amiro, B., Ammann, C., Arain, M. A., Ardo, J., Arkebauer, T., Arndt, S. K., Arriga, N., Aubinet, M., Aurela, M., Baldocchi, D., Barr, A., Beamesderfer, E., Marchesini, L. B., Bergeron, O., Beringer, J., Bernhofer, C., Berveiller, D., Billesbach, D., Black, T. A., Blanken, P. D., Bohrer, G., Boike, J., Bolstad, P. V., Bonal, D., Bonnefond, J., Bowling, D. R., Bracho, R., Brodeur, J., Bruemmer, C., Buchmann, N., Burban, B., Burns, S. P., Buysse, P., Cale, P., Cavagna, M., Cellier, P., Chen, S., Chini, I., Christensen, T. R., Cleverly, J., Collalti, A., Consalvo, C., Cook, B. D., Cook, D., Coursolle, C., Cremonese, E., Curtis, P. S., D'Andrea, E., Rocha, H. D., Dai, X., Davis, K. J., De Cinti, B., de Grandcourt, A., De Ligne, A., De Oliveira, R. C., Delpierre, N., Desai, A. R., Di Bella, C. M., di Tommasi, P., Dolman, H., Domingo, F., Dong, G., Dore, S., Duce, P., Dufrene, E., Dunn, A., Dusek, J., Eamus, D., Eichelmann, U., Elkhidir, H. A. M., Eugster, W., Ewenz, C. M., Ewers, B., Famulari, D., Fares, S., Feigenwinter, I., Feitz, A., Fensholt, R., Filippa, G., Fischer, M., Frank, J., Galvagno, M., Gharun, M., Gianelle, D., Gielen, B., Gioli, B., Gitelson, A., Goded, I., Goeckede, M., Goldstein, A. H., Gough, C. M., Goulden, M. L., Graf, A., Griebel, A., Gruening, C., Gruenwald, T., Hammerle, A., Han, S., Han, X., Hansen, B. U., Hanson, C., Hatakka, J., He, Y., Hehn, M., Heinesch, B., Hinko-Najera, N., Hoertnagl, L., Hutley, L., Ibrom, A., Ikawa, H., Jackowicz-Korczynski, M., Janous, D., Jans, W., Jassal, R., Jiang, S., Kato, T., Khomik, M., Klatt, J., Knohl, A., Knox, S., Kobayashi, H., Koerber, G., Kolle, O., Kosugi, Y., Kotani, A., Kowalski, A., Kruijt, B., Kurbatova, J., Kutsch, W. L., Kwon, H., Launiainen, S., Laurila, T., Law, B., Leuning, R., Li, Y., Liddell, M., Limousin, J., Lion, M., Liska, A. J., Lohila, A., Lopez-Ballesteros, A., Lopez-Blanco, E., Loubet, B., Loustau, D., Lucas-Moffat, A., Lueers, J., Ma, S., Macfarlane, C., Magliulo, V., Maier, R., Mammarella, I., Manca, G., Marcolla, B., Margolis, H. A., Marras, S., Massman, W., Mastepanov, M., Matamala, R., Matthes, J. H., Mazzenga, F., Mccaughey, H., Mchugh, I., Mcmillan, A. M. S., Merbold, L., Meyer, W., Meyers, T., Miller, S. D., Minerbi, S., Moderow, U., Monson, R. K., Montagnani, L., Moore, C. E., Moors, E., Moreaux, V., Moureaux, C., Munger, J. W., Nakai, T., Neirynck, J., Nesic, Z., Nicolini, G., Noormets, A., Northwood, M., Nosetto, M., Nouvellon, Y., Novick, K., Oechel, W., Olesen, J. E., Ourcival, J., Papuga, S. A., Parmentier, F., Paul-Limoges, E., Pavelka, M., Peichl, M., Pendall, E., Phillips, R. P., Pilegaard, K., Pirk, N., Posse, G., Powell, T., Prasse, H., Prober, S. M., Rambal, S., Rannik, U., Raz-Yaseef, N., Reed, D., de Dios, V. R., Restrepo-Coupe, N., Reverter, B. R., Roland, M., Sabbatini, S., Sachs, T., Saleska, S. R., Sanchez-Canete, E. P., Sanchez-Mejia, Z. M., Schmid, H. P., Schmidt, M., Schneider, K., Schrader, F., Schroder, I., Scott, R. L., Sedlak, P., Serrano-Ortiz, P., Shao, C., Shi, P., Shironya, I., Siebicke, L., Sigut, L., Silberstein, R., Sirca, C., Spano, D., Steinbrecher, R., Stevens, R. M., Sturtevant, C., Suyker, A., Tagesson, T., Takanashi, S., Tang, Y., Tapper, N., Thom, J., Tiedemann, F., Tomassucci, M., Tuovinen, J., Urbanski, S., Valentini, R., van der Molen, M., van Gorsel, E., van Huissteden, K., Varlagin, A., Verfaillie, J., Vesala, T., Vincke, C., Vitale, D., Vygodskaya, N., Walker, J. P., Walter-Shea, E., Wang, H., Weber, R., Westermann, S., Wille, C., Wofsy, S., Wohlfahrt, G., Wolf, S., Woodgate, W., Li, Y., Zampedri, R., Zhang, J., Zhou, G., Zona, D., Agarwal, D., Biraud, S., Torn, M., and Papale, D.: The

FLUXNET2015 dataset and the ONEFlux processing pipeline for eddy covariance data, Sci. Data, 7, 27, https://doi.org/10.1038/s41597-020-0534-3, 2020.

Pei, Y., Dong, J., Zhang, Y., Yang, J., Wu, S., Gay, B. A., He, B., and Xiao, X.: Sensitivity of dryland plant water availability to changes in carbon and water fluxes, J. Hydrol., 662, 11, https://doi.org/10.1016/j.jhydrol.2025.133966, 2025.

Qin, Y., Wang, D., Cao, Y., Cai, X., Liang, S., Beck, H. E., and Zeng, Z.: Sub-grid representation of vegetation cover in land surface schemes improves the modeling of how climate responds to deforestation, Geophys. Res. Lett., 50, 10, https://doi.org/10.1029/2023GL104164, 2023.

Robinson, N. P., Allred, B. W., Smith, W. K., Jones, M. O., Moreno, A., Erickson, T. A., Naugle, D. E., and Running, S. W.: Terrestrial primary production for the conterminous united states derived from landsat 30 m and MODIS 250 m, Remote Sens. Ecol. Conserv., 4, 264-280, https://doi.org/10.1002/rse2.74, 2018.

Ruehr, S., Gerlein-Safdi, C., Falco, N., Seibert, P. O., Chou, C., Albert, L., and Keenan, T. F.: Quantifying seasonal and diurnal cycles of solar-induced fluorescence with a novel hyperspectral imager, Geophys. Res. Lett., 51, 11, https://doi.org/10.1029/2023GL107429, 2024.

Ruehr, S., Keenan, T. F., Williams, C., Zhou, Y., Lu, X., Bastos, A., Canadell, J. G., Prentice, I. C., Sitch, S., and Terrer, C.: Evidence and attribution of the enhanced land carbon sink, Nat. Rev. Earth Environ., 4, 518-534, https://doi.org/10.1038/s43017-023-00456-3, 2023.

Runge, J., Bathiany, S., Bollt, E., Camps-Valls, G., Coumou, D., Deyle, E., Glymour, C., Kretschmer, M., Mahecha, M. D., Munoz-Mari, J., van Nes, E. H., Peters, J., Quax, R., Reichstein, M., Scheffer, M., Schoelkopf, B., Spirtes, P., Sugihara, G., Sun, J., Zhang, K., and Zscheischler, J.: Inferring causation from time series in earth system sciences, Nat. Commun., 10, 13, https://doi.org/10.1038/s41467-019-10105-3, 2019.

Runge, J., Gerhardus, A., Varando, G., Eyring, V., and Camps-Valls, G.: Causal inference for time series, Nat. Rev. Earth Environ., 4, 487-505, https://doi.org/10.1038/s43017-023-00431-y, 2023.

Runge, J., Nowack, P., Kretschmer, M., Flaxman, S., and Sejdinovic, D.: Detecting and quantifying causal associations in large nonlinear time series datasets, Sci. Adv., 5, 15, https://doi.org/10.1126/sciadv.aau4996, 2019.

Ryu, Y., Berry, J. A., and Baldocchi, D. D.: What is global photosynthesis? History, uncertainties and opportunities, Remote Sens. Environ., 223, 95-114, https://doi.org/10.1016/j.rse.2019.01.016, 2019.

Seferian, R., Nabat, P., Michou, M., Saint-Martin, D., Voldoire, A., Colin, J., Decharme, B., Delire, C., Berthet, S., Chevallier, M., Senesi, S., Franchisteguy, L., Vial, J., Mallet, M., Joetzjer, E., Geoffroy, O., Gueremy, J., Moine, M., Msadek, R., Ribes, A., Rocher, M., Roehrig, R., Salas-Y-Melia, D., Sanchez, E., Terray, L., Valcke, S., Waldman, R., Aumont, O., Bopp, L., Deshayes, J., Ethe, C., and Madec, G.: Evaluation of CNRM earth system model , CNRM - ESM2 - 1 : role of earth system processes in present-day and future climate, J. Adv. Model. Earth Syst., 11, 4182-4227, https://doi.org/10.1029/2019MS001791, 2019.

Stavros, E. N., Schimel, D., Pavlick, R., Serbin, S., Swann, A., Duncanson, L., Fisher, J. B., Fassnacht, F., Ustin, S., Dubayah, R., Schweiger, A., and Wennberg, P.: ISS observations offer insights into plant function, Nat. Ecol. Evol., 1, 4, https://doi.org/10.1038/s41559-017-0194, 2017.

Taylor, T. E., Eldering, A., Merrelli, A., Kiel, M., Somkuti, P., Cheng, C., Rosenberg, R., Fisher, B., Crisp, D., Basilio, R., Bennett, M., Cervantes, D., Chang, A., Dang, L., Frankenberg, C., Haemmerle, V. R., Keller, G. R., Kurosu, T., Laughner, J. L., Lee, R., Marchetti, Y., Nelson, R. R., O'Dell, C. W., Osterman, G., Pavlick, R., Roehl, C., Schneider, R., Spiers, G., To, C., Wells, C., Wennberg, P. O., Yelamanchili, A., and Yu, S.: OCO-3 early mission operations and initial (vearly) XCO 2 and SIF retrievals, Remote Sens. Environ., 251, 27, https://doi.org/10.1016/j.rse.2020.112032, 2020.

Voldoire, A., Saint-Martin, D., Sénési, S., Decharme, B., Alias, A., Chevallier, M., Colin, J., Guérémy, J. F., Michou, M., Moine, M. P., Nabat, P., Roehrig, R., Mélia, D., Séférian, R., Valcke, S., Beau, I., Belamari, S., Berthet, S., Cassou, C., Cattiaux, J., Deshayes, J., Douville, H., Ethé, C., Franchistéguy, L., Geoffroy, O., Lévy, C., Madec, G., Meurdesoif, Y., Msadek, R., Ribes, A., Sanchez-Gomez, E., Terray, L., and Waldman, R.: Evaluation of CMIP6 DECK experiments with CNRM-CM6-1, J. Adv. Model. Earth Syst., 11, 2177-2213, https://doi.org/10.1029/2019MS001683, 2019.

Wang, B., Yue, X., Zhou, H., Lu, X., and Zhu, J.: Enhanced ecosystem water-use efficiency under the more diffuse radiation conditions, Glob. Biogeochem. Cycle, 37, 14, https://doi.org/10.1029/2022GB007606, 2023.

Wang, J.: Global daily 1 km gapless XCO 2 (2003-2023) derived from multi-satellite observations and a spatiotemporal deep learning framework, Environ. Impact Assess. Rev., 117, 22, https://doi.org/10.1016/j.eiar.2025.108146, 2026.

Wang, J., Hua, H., Guo, J., Huang, X., Zhang, X., Yang, Y., Wang, D., Guo, X., Zhang, R., Smith, N. G., Rossi, S., Penuelas, J., Ciais, P., Wu, C., and Chen, L.: Late spring frost delays tree spring phenology by reducing photosynthetic productivity, Nat. Clim. Chang., 15, 18, https://doi.org/10.1038/s41558-024-02205-w, 2025.

Wang, X., Guo, Z., Zhang, K., Fu, Z., Lee, C. K. F., Yang, D., Detto, M., Zhang, Y., and Wu, J.: Can large-scale satellite products track the effects of atmospheric dryness and soil water deficit on ecosystem productivity under droughts? Geophys. Res. Lett., 52, 12, https://doi.org/10.1029/2024GL110785, 2025.

Wei, S., Fang, H., Schaaf, C. B., He, L., and Chen, J. M.: Global 500 m clumping index product derived from MODIS BRDF data (2001-2017), Remote Sens. Environ., 232, 15, https://doi.org/10.1016/j.rse.2019.111296, 2019.

Wilson, K. B., Baldocchi, D., Falge, E., Aubinet, M., Berbigier, P., Bernhofer, C., Dolman, H., Field, C., Goldstein, A., Granier, A., Hollinger, D., Katul, G., Law, B. E., Meyers, T., Moncrieff, J., Monson, R., Tenhunen, J., Valentini, R., Verma, S., and Wofsy, S.: Diurnal centroid of ecosystem energy and carbon fluxes at FLUXNET sites - art. No. 4664, J. Geophys. Res.-Atmos., 108, 13, https://doi.org/10.1029/2001JD001349, 2003.

Xiao, J., Baldocchi, D., Ichii, K., Li, F., and Papale, D.: Insights into terrestrial carbon and water cycling from the global eddy covariance network, Nat. Rev. Earth Environ., 20, https://doi.org/10.1038/s43017-025-00743-1, 2025.

Xiao, J., Chevallier, F., Gomez, C., Guanter, L., Hicke, J. A., Huete, A. R., Ichii, K., Ni, W., Pang, Y., Rahman, A. F., Sun, G., Yuan, W., Zhang, L., and Zhang, X.: Remote sensing of the terrestrial carbon cycle: a review of advances over 50 years, Remote Sens. Environ., 233, 37, https://doi.org/10.1016/j.rse.2019.111383, 2019.

Xiao, J., Fisher, J. B., Hashimoto, H., Ichii, K., and Parazoo, N. C.: Emerging satellite observations for diurnal cycling of ecosystem processes, Nat. Plants, 7, 877-887, https://doi.org/10.1038/s41477-021-00952-8, 2021.

Yuan, K., Li, F., Mcnicol, G., Chen, M., Hoyt, A., Knox, S., Riley, W. J., Jackson, R., and Zhu, Q.: Boreal-arctic wetland methane emissions modulated by warming and vegetation activity, Nat. Clim. Chang., 14, 10, https://doi.org/10.1038/s41558-024-01933-3, 2024.

Yuan, K., Zhu, Q., Li, F., Riley, W. J., Torn, M., Chu, H., Mcnicol, G., Chen, M., Knox, S., Delwiche, K., Wu, H., Baldocchi, D., Ma, H., Desai, A. R., Chen, J., Sachs, T., Ueyama, M., Sonnentag, O., Helbig, M., Tuittila, E., Jurasinski, G., Koebsch, F., Campbell, D., Schmid, H. P., Lohila, A., Goeckede, M., Nilsson, M. B., Friborg, T., Jansen, J., Zona, D., Euskirchen, E., Ward, E. J., Bohrer, G., Jin, Z., Liu, L., Iwata, H., Goodrich, J., and Jackson, R.: Causality guided machine learning model on wetland CH 4 emissions across global wetlands, Agric. For. Meteorol., 324, 10, https://doi.org/10.1016/j.agrformet.2022.109115, 2022.

Zeng, Y., Hao, D., Huete, A., Dechant, B., Berry, J., Chen, J. M., Joiner, J., Frankenberg, C., Bond-Lamberty, B., Ryu, Y., Xiao, J., Asrar, G. R., and Chen, M.: Optical vegetation indices for monitoring terrestrial ecosystems globally, Nat. Rev. Earth Environ., 3, 477-493, https://doi.org/10.1038/s43017-022-00298-5, 2022.

Zhang, Y., Feng, X., Zhou, C., Sun, C., Leng, X., and Fu, B.: Aridity threshold of ecological restoration mitigated atmospheric drought via land-atmosphere coupling in drylands, Commun. Earth Environ., 5, 11, https://doi.org/10.1038/s43247-024-01555-9, 2024.

Zhang, Z., Cescatti, A., Wang, Y., Gentine, P., Xiao, J., Guanter, L., Huete, A. R., Wu, J., Chen, J. M., Ju, W., Penuelas, J., and Zhang, Y.: Large diurnal compensatory effects mitigate the response of amazonian forests to atmospheric warming and drying, Sci. Adv., 9, 15, https://doi.org/10.1126/sciadv.abq4974, 2023.

Zhang, Z., Guanter, L., Porcar-Castell, A., Rossini, M., Labrador, J. P., and Zhang, Y.: Global modeling diurnal gross primary production from OCO-3 solar-induced chlorophyll fluorescence, Remote Sens. Environ., 285, 15, https://doi.org/10.1016/j.rse.2022.113383, 2023.

Zhang, Z., Lu, L., Zhao, Y., Wang, Y., Wei, D., Wu, X., and Ma, X.: Recent advances in using chinese earth observation satellites for remote sensing of vegetation, ISPRS-J. Photogramm. Remote Sens., 195, 393-407, https://doi.org/10.1016/j.isprsjprs.2022.12.006, 2023.

Zhao, C. and Zhu, W.: Vegetation structure and phenology primarily shape the spatiotemporal pattern of ecosystem respiration, Commun. Earth Environ., 6, 15, https://doi.org/10.1038/s43247-025-02240-1, 2025.

Zhao, C., Zhu, W., Chen, L., and Xie, Z.: Causality constrained machine learning framework enhances the reliability and spatiotemporal generalization in ecosystem respiration estimation, Agric. For. Meteorol., 372, 16, https://doi.org/10.1016/j.agrformet.2025.110718, 2025.

Zhao, M. S., Heinsch, F. A., Nemani, R. R., and Running, S. W.: Improvements of the MODIS terrestrial gross and net primary production global data set, Remote Sens. Environ., 95, 164-176, https://doi.org/10.1016/j.rse.2004.12.011, 2005.

Zhu, Z. and Zhu, X.: Increasing midday depression of mangrove photosynthesis with heat and drought stresses, Agric. For. Meteorol., 362, 9, https://doi.org/10.1016/j.agrformet.2024.110372, 2025.

Zomer, R. J., Xu, J., and Trabucco, A.: Version 3 of the global aridity index and potential evapotranspiration database, Sci. Data, 9, 15, https://doi.org/10.1038/s41597-022-01493-1, 2022.